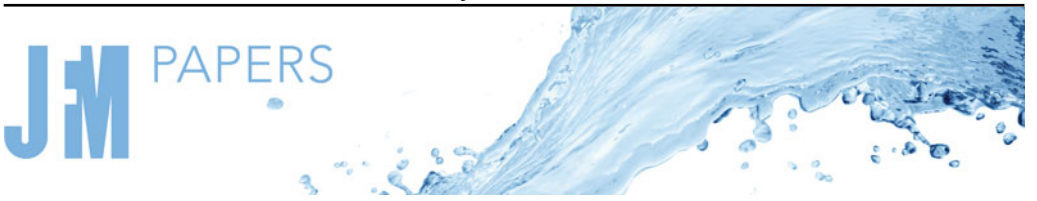
J. Fluid Mech. (2025), *vol.* 1011, A21, doi:10.1017/jfm.2025.365



Near-wall effect on vortex dynamics in the flow around a rectangular cylinder

Jiang-Hua Li[1,2,3,4], **Bo-Fu Wang**[3], **Xiang Qiu**[3,4], **Quan Zhou**[3], **Shi-Xiao Fu**[1,2] **and Yu-Lu Liu**[3,4]

[1]State Key Laboratory of Ocean Engineering, Shanghai Jiao Tong University, Shanghai 200040, PR China

[2]School of Ocean and Civil Engineering, Shanghai Jiao Tong University, Shanghai 200240, PR China

[3]Shanghai Key Laboratory of Mechanics in Energy Engineering, Shanghai Institute of Applied Mathematics and Mechanics, School of Mechanics and Engineering Science, Shanghai University, Shanghai 200072, PR China

[4]School of Science, Shanghai Institute of Technology, Shanghai 201418, PR China

Corresponding authors: Bo-Fu Wang, bofuwang@shu.edu.cn; Shi-Xiao Fu, shixiao.fu@sjtu.edu.cn

(Received 15 November 2024; revised 31 January 2025; accepted 28 March 2025)

This study presents a novel investigation into the vortex dynamics of flow around a near-wall rectangular cylinder based on direct numerical simulation at $Re = 1000$, marking the first in-depth exploration of these phenomena. By varying aspect ratios ($L/D = 5$, 10, 15) and gap ratios ($G/D = 0.1$, 0.3, 0.9), the study reveals the vortex dynamics influenced by the near-wall effect, considering the incoming laminar boundary layer flow. Both L/D and G/D significantly influence vortex dynamics, leading to behaviours not observed in previous bluff body flows. As G/D increases, the streamwise scale of the upper leading edge (ULE) recirculation grows, delaying flow reattachment. At smaller G/D, lower leading edge (LLE) recirculation is suppressed, with upper Kelvin–Helmholtz vortices merging to form the ULE vortex, followed by instability, differing from conventional flow dynamics. Larger G/D promotes the formation of an LLE shear layer. An intriguing finding at $L/D = 5$ and $G/D = 0.1$ is the backward flow of fluid from the downstream region to the upper side of the cylinder. At $G/D = 0.3$, double-trailing-edge vortices emerge for larger L/D, with two distinct flow behaviours associated with two interactions between gap flow and wall recirculation. These interactions lead to different multiple flow separations. For $G/D = 0.9$, the secondary vortex (SV) from the plate wall induces the formation of a tertiary vortex from the lower side of the cylinder. Double-SVs are observed at $L/D = 5$. Frequency locking is observed in most cases, but is suppressed at $L/D = 10$ and $G/D = 0.9$, where competing shedding modes lead to two distinct evolutions of the SV.

Key words: boundary layer separation, vortex dynamics, vortex interactions

© The Author(s), 2025. Published by Cambridge University Press.

https://doi.org/10.1017/jfm.2025.365 Published online by Cambridge University Press

1. Introduction

The flow around bluff bodies positioned transversely near a planar wall has garnered significant interest in fluid mechanics due to its fundamental and practical importance (Squire 1989; Ovchinnikov, Piomelli & Choudhari 2006; Maiti 2012; Malavasi & Blois 2012; Kukreti & Singh 2023). However, notable differences exist in the simplified models of blunt bodies across various engineering applications. For instance, the subsea oil and gas pipelines are often modelled as circular cylinders in proximity to a wall, whereas vehicles such as cars and trains, as well as some buildings, are typically represented as elongated rectangular cylinders near a wall. The flow characteristics around a rectangular cylinder differ markedly from those around a circular cylinder, with the former exhibiting phenomena such as shear layer separation and subsequent reattachment (Cimarelli *et al.* 2018*a*, 2019*a*; Chiarini & Quadrio 2021), which are less pronounced in flows involving circular geometries. Consequently, understanding the vortex dynamics in the flow around near-wall bluff bodies is crucial for elucidating fundamental aspects of fluid mechanics. The present study primarily investigates the flow characteristics around a near-wall rectangular cylinder (FNRC), exploring the influence of near-wall effects on the flow around the rectangular cylinder.

The interaction between the wake of a circular cylinder and the boundary layer of a plate wall has been extensively studied in both experimental (Bearman & Zdravkovich 1978; Zdravkovich 1985; Lei, Cheng & Kavanagh 1999; Price *et al.* 2002; Wang & Tan 2008; He, Pan & Wang 2013*a*, 2017; Wang, He & Wang 2024) and numerical simulations (Lei *et al.* 2000; Sarkar & Sarkar 2009, 2010; Ouro, Muhawenimana & Wilson 2019; Chen *et al.* 2022; Li *et al.* 2022*a*,*b*). These investigations reveal that the flow around a near-wall circular cylinder (FNCC) is primarily influenced by several key parameters, including the gap ratio G/D (where G is the distance from the wall to the bottom side of the cylinder and D is the cylinder thickness), the Reynolds number $Re = U_0 D/\nu$ (with U_0 as the fixed free stream velocity outside the plate boundary layer and ν as the kinematic viscosity) and the plate boundary layer thickness δ_D/D (where δ_D is the boundary layer thickness at the position of the cylinder in the absence of the cylinder). Among these parameters, G/D is particularly critical, as it governs the vortex dynamics of the FNCC.

A prominent phenomenon observed in the FNCC in the subcritical regime of $Re \sim 10^3 - 10^5$ is the induction of plate boundary layer separation by the wake vortex at certain gap ratios, leading to the formation of a secondary vortex (SV) structure that rotates in the same direction as the upper wake vortex. The interaction between the wake vortex and the SV is significantly influenced by G/D. For $G/D \leqslant 0.125$, the alternate vortex shedding from the upper and lower sides of the cylinder is suppressed (Price *et al.* 2002; Li *et al.* 2022*a*). Price *et al.* (2002) noted the presence of periodicity in the upper shear layer, despite the absence of regular vortex shedding. This periodicity has been attributed to the Kelvin–Helmholtz (KH) instability in the upper shear layer, resulting in the formation of KH vortices, as demonstrated in the study by Li *et al.* (2022*a*). Furthermore, Li *et al.* (2022*a*) observed that the KH vortex evolves into hairpin vortices downstream due to secondary instability. For the range $0.25 \leqslant G/D \leqslant 0.5$, the SV forms from the wall boundary layer as a result of the wake vortex induction. This is followed by complex interactions among the upper wake vortex, the lower wake vortex and the SV (Price *et al.* 2002; Sarkar & Sarkar 2009, 2010; He *et al.* 2017; Li *et al.* 2022*a*; Zhou *et al.* 2022). During these interactions, the lower wake vortex breaks up, while the SV rises and merges with the upper wake vortex. This merging leads to the development of hairpin vortices and braid vortices (Li *et al.* 2022*a*). In the range $0.7 \leqslant G/D \leqslant 1.0$, the interactions between vortices diminish, as the SV interacts only with the lower wake

https://doi.org/10.1017/jfm.2025.365 Published online by Cambridge University Press

vortex, leaving the upper wake vortex uninvolved (Price *et al.* 2002; He *et al.* 2013*a*,*b*; Li *et al.* 2022*a*). Additionally, the hairpin vortex evolves from the SV, but its head becomes entrained into the wake (Li *et al.* 2022*a*). As the gap ratio increases to $G/D = 2 - 3$, the SV can still form periodically. However, there is no direct interaction between the SV and the wake vortices. The SV can also develop into hairpin vortices (He *et al.* 2016, 2017). During these varying interactions, Li *et al.* (2022*a*) identified a tertiary vortex (TV), which is induced by the SV and rotates in the opposite direction. Notably, the characteristic frequency f of the TV matches that of the wake vortices along with the SV. Recently, Jiang *et al.* (2024) investigated the flow around a circular cylinder in proximity to a moving wall for $Re = 300 - 1000$ and $G/D = 0.2 - 3$. The moving wall eliminates the boundary layer while retaining a near-wall effect, thereby elucidating several flow characteristics documented in the literature for a stationary wall. By comparing flows between stationary and moving walls, they found that the development of the upstream wall boundary layer significantly affects the flows, particularly leading to an increase in the Strouhal number $St = fD/U_0$ for a stationary wall for $G/D = 0.5 - 2$.

Compared with the flow around a circular cylinder, the flow around a rectangular cylinder introduces an additional parameter: the aspect ratio L/D (where L represents the streamwise dimension of the rectangular cylinder). The flow around an isolated rectangular cylinder (FIRC) exhibits distinct features depending on the value of L/D and has garnered significant interest from researchers over the years. When L/D is sufficiently large ($L/D > 3$), the shear layer developing from the leading edge (LE) can reattach to the upper and lower sides of the rectangular cylinder, resulting in flow separation at the trailing edge (TE). Consequently, the LE vortices and TE vortices can form separately for $Re > 300$. Notably, the shedding frequency of these vortices is the same, indicating a phenomenon known as frequency locking, which is a key characteristic of vortex dynamics in the flow around a rectangular cylinder. In the FIRC, two distinct increases in the new Strouhal number $St(L) = fL/U_0$ are observed as L/D increases. The first increase occurs in a stepwise manner, dominated by the LE vortex (Okajima 1982; Nakamura, Ohya & Tsuruta 1991; Ozono *et al.* 1992; Mills *et al.* 1995; Tan, Thompson & Hourigan 1998; Chiarini *et al.* 2022*c*; Zhang *et al.* 2023). In contrast, the second increase of $St(L)$ rises almost linearly with L/D (Chiarini *et al.* 2022*c*). To elucidate the frequency locking and the stepwise dependence of $St(L)$, studies on the impinging shear layer instability (Nakamura & Nakashima 1986) and the impinging LE vortex instability (Nakamura *et al.* 1991; Naudascher & Rockwell 1994; Mills, Sheridan & Hourigan 2002; Tan, Thompson & Hourigan 2004; Chiarini *et al.* 2022*c*) have been conducted, respectively. Recently, Chiarini, Quadrio & Auteri (2021) identified that the primary instability is attributed to a Hopf bifurcation at low Re. Furthermore, Chiarini *et al.* (2022*b*) discovered a new quasisubharmonic unstable mode at $L/D = 5$, with the wavemaker region located on the upper and lower sides of the rectangular cylinder. This three-dimensional (3-D) instability arises from the mutual inviscid interaction of vortices originating from the LE shear layer. Moreover, Zhang *et al.* (2023) concentrated on global instability and identified the phase difference between the LE and TE vortices as a critical factor contributing to the stepwise growth of $St(L)$ as L/D increases. They demonstrated that self-sustained oscillations are maintained by two types of pressure feedback-loop mechanisms (Hourigan, Thompson & Tan 2001): the flow exhibits the impinging shear layer instability at $L/D = 4$ and 5, while it is characterized by the impinging LE vortex instability for $L/D = 3$ and 6–12.

Regarding the vortex dynamics of the flow around a rectangular cylinder, Chiarini *et al.* (2022*c*) identified that the shedding dynamics of the TE vortex are pivotal in the phenomenon of frequency locking at $Re = 400$. They found two distinct configurations

https://doi.org/10.1017/jfm.2025.365 Published online by Cambridge University Press

in the two-dimensional flow, which exhibit a significant correlation with the interaction between the LE and TE vortices. At a medium Reynolds number ($Re = 1000$), Li *et al.* (2024*b*) discovered a fractional harmonic in the 3-D flow, revealing that it arises from the feedback effect resulting from the interaction between the reverse boundary layer and the upstream development of the split LE shear layer. They also identified two shedding patterns – ipsilateral and contralateral vortex shedding – at different L/D, similar to the configurations found by Chiarini *et al.* (2022*c*). Notably, contralateral vortex shedding can suppress Kármán-type vortex development in the wake. Additionally, Li *et al.* (2024*a*) further evaluated the connection between crucial vortices and turbulent transport. For high Reynolds numbers ($Re \geqslant 3000$), previous studies have predominantly focused on the flow for $L/D = 5$. This flow is characterized by quasistreamwise vortices and streamwise streaks on the upper and lower sides (Cimarelli *et al.* 2018*b*). The self-sustaining mechanisms of the flow have been derived, showing that large-scale pressure fluctuations alternate between promoting and suppressing the reverse flow. Driven by large-scale dynamics, small-scale motions trigger the LE shear layer, which subsequently creates vortices that alternate between the upper and lower sides of the cylinder, resulting in a relatively long period of inversion and thus closing the self-sustaining cycle. Cimarelli *et al.* (2019*a*,*b*), Chiarini & Quadrio (2021) and Chiarini *et al.* (2022*a*) also studied spatial and interscale energy transport to understand the evolutionary behaviour of turbulent vortex structures. Furthermore, Cimarelli, Corsini & Stalio (2024) provided a detailed analysis of this flow at $Re = 3000$, 8000 and 14 000, encompassing the laminar boundary layer on the front face, the separated shear layer, flow impingement at reattachment, the reverse boundary layer and near- and far-wake flow. The physics of these phenomena are elaborated, including the slow modulation induced by large-scale instabilities associated with vortex shedding. The literature review suggests that the flow around a rectangular cylinder exhibits more diverse flow features than that around a circular cylinder, garnering considerable attention in the research community.

The FNRC is commonly encountered in engineering applications, as previously described. However, most prior research focused on circular cylinders when examining bluff bodies near a wall. Additionally, the near-wall effect on the vortex dynamics in the FNRC is expected to be more complex. Although some studies have been conducted on this flow, most have concentrated on configurations where $0.1 \leqslant L/D \leqslant 2$ (Maiti 2012; Tanweer *et al.* 2021, 2022). Recently, Chiarini & Auteri (2023) investigated the primary instability of the steady two-dimensional flow past rectangular cylinders moving parallel to a wall at $Re \leqslant 300$, neglecting the influence of the wall boundary layer. Consequently, the vortex dynamics of the FNRC warrants further investigation, particularly in terms of its similarities and differences with the FNCC and FIRC.

In this work, we delve into the vortex dynamics in the flow around a rectangular cylinder positioned near a plate, including the intricate interactions between the plate boundary layer and the LE/TE vortex shed from the rectangular cylinder. To the best of the authors' knowledge, such research has not been previously reported. The investigation is conducted using direct numerical simulation (DNS) at a medium Reynolds number ($Re = 1000$). Three aspect ratios ($L/D = 5$, 10 and 15) and gap ratios ($G/D = 0.1$, 0.3 and 0.9) are considered. This study is expected to enhance the physical understanding of vortex dynamics, thereby improving insights into the flow physics around a near-wall blunt body. The structure of the paper is organized as follows: § 2 presents the physical model, numerical methods, and data analysis techniques; the main findings are discussed in § 3; finally, § 4 provides the conclusions drawn from this study.

https://doi.org/10.1017/jfm.2025.365 Published online by Cambridge University Press

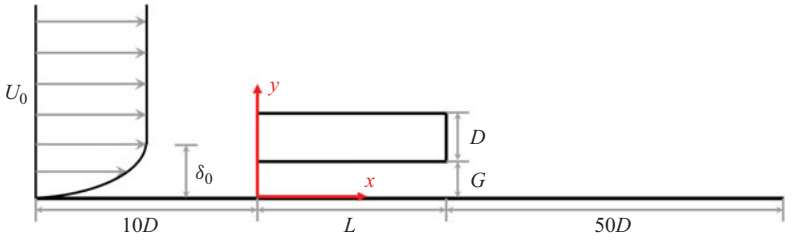


Figure 1. The sketch of FNRC in a $x-y$ plane. Here L and D are the streamwise and wall-normal dimensions of the rectangular cylinder. The gap G is the distance from the wall to the bottom side of the cylinder. Here U_0 is the inflow velocity; δ_0 is the wall boundary layer thickness at the inlet.

2. Numerical model

2.1. *Flow configuration and numerical method*

In the present study, 3-D DNS are performed to investigate the flow around a rectangular cylinder positioned transversely near a plate wall. The sketch of this flow configuration is presented in figure 1, where L and D represent the streamwise and wall-normal dimensions of the rectangular cylinder, respectively, and G denotes the gap between the plate wall and the lower side of the cylinder. Following the studies of Li *et al.* (2022*a*) and Li *et al.* (2024*b*), the computational domain is defined as $-10D \leqslant x \leqslant L + 50D$ in the streamwise direction, $0 \leqslant y \leqslant 15D$ in the wall-normal direction and $0 \leqslant z \leqslant 2\pi D$ in the spanwise direction. To explore the near-wall effect on the flow and to compare the vortex dynamics with that in the FNCC (Li *et al.* 2022*a*) and FIRC (Li *et al.* 2024*b*), the Reynolds number is fixed at 1000. The study considers three aspect ratios ($L/D = 5$, 10, 15) and small gap ratios ($G/D = 0.1$, 0.3, 0.9). The governing equations consist of the continuity and incompressible Navier–Stokes equations in their dimensionless form, expressed as follows:

$$\nabla \cdot \mathbf{u} = 0, \tag{2.1}$$

$$\frac{\partial \mathbf{u}}{\partial t} + \mathbf{u} \cdot \bigtriangledown \mathbf{u} = -\nabla p + \frac{1}{Re}\nabla^2 \mathbf{u}, \tag{2.2}$$

where, $\mathbf{u} \equiv (u, v, w)$ is velocity vector, t is time and p is pressure. The Reynolds number is also defined as $Re = U_0 D/\nu$, where D is the cylinder thickness and U_0 is the free stream streamwise velocity outside the plate boundary layer. Equations (2.1) and (2.2) are solved using the unsteady incompressible Navier–Stokes solver embedded in the open-source code Nektar++ (Cantwell *et al.* 2015; Moxey *et al.* 2020). This solver utilizes the Fourier spectral/hp element method (Bolis 2013) and has been widely employed in studies of flow around bluff bodies (Ju *et al.* 2020; Jiang *et al.* 2022; Li *et al.* 2023; Ren *et al.* 2023; Ju & Jiang 2024).

A laminar flow profile, based on the Blasius similarity solution, is imposed at the inlet (Li *et al.* 2022*a*,*b*; Feng *et al.* 2024), resulting in a boundary layer thickness of $\delta_0 = 0.492D$. The far field conditions, defined as $\partial u/\partial y = 0$, $v = 0$ and $\partial w/\partial y = 0$, are applied along the upper surface of the computational domain. No-slip boundary conditions ($u = v = w = 0$) are enforced on the surfaces of the rectangular cylinder and the plate wall (the lower surface of the domain). At the outlet, a high-order outflow boundary condition is implemented (Dong, Karniadakis & Chryssostomidis 2014). A second-order implicit–explicit time integration scheme is chosen from the incompressible solver, and the time

https://doi.org/10.1017/jfm.2025.365 Published online by Cambridge University Press

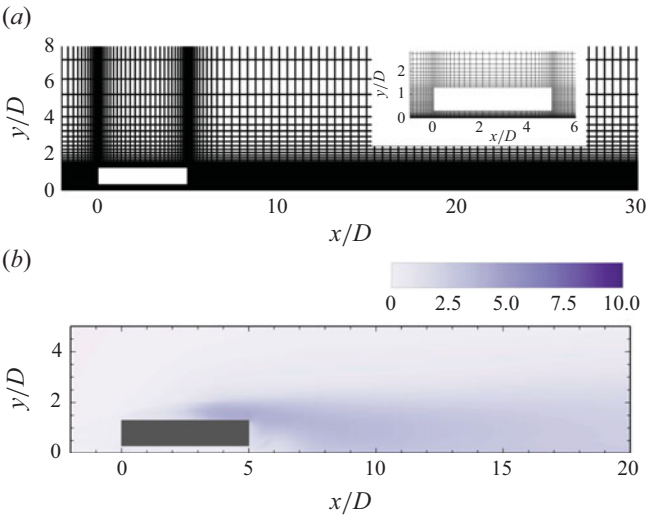


Figure 2. (*a*) The partial domain with a macro mesh for $L/D = 5$, $G/D = 0.3$ in the $x-y$ plane. The inset is a close-up view of the mesh near the rectangular cylinder. (*b*) The ratio of the grid size to the Kolmogorov length scale (Δ/η) in the $x-y$ plane for $L/D = 5$ and $G/D = 0.3$.

step is fixed at 0.001. The problem is spatially discretized in the $x-y$ plane, combined with the Fourier expansion in the z direction to capture the 3-D characteristics of the flow, based on the assumption of homogeneity in the spanwise direction (Bolis 2013). In the spanwise direction, $N = 96$ Fourier planes are utilized, as referenced in the studies by Li *et al.* (2022*a*) and Li *et al.* (2024*b*) with the same Re. In the $x-y$ plane, the spatial resolution is determined by the distribution of h-type elements, and the macromesh for $L/D = 5$, $G/D = 0.3$ is shown in figure 2(*a*).

The reliability of Nektar++ has been well-established in previous studies of the FNCC (Li *et al.* 2022*a*,*b*) and FIRC (Li *et al.* 2024*a*,*b*) at $Re = 1000$. In this study, the FNRC is investigated for the first time with a large L/D. To ensure the accuracy of the numerical results, a mesh independence study is conducted by evaluating the convergence of the drag coefficient $C_D = 2F_x/\rho D U_0^2$ and the lift coefficient $C_L = 2F_y/\rho L U_0^2$, where F_x and F_y represent the spanwise-averaged total forces acting on the cylinder in the streamwise and wall-normal directions, respectively. The mean drag and lift coefficients ($\overline{C_D}$ and $\overline{C_L}$) for different polynomial orders P are presented in table 1, using the typical case of $L/D = 5$ and $G/D = 0.3$. Four meshes are generated with P (the order interpolation polynomials for the p-type expansion) varying from 4 to 7. It can be observed that $\overline{C_D}$ and $\overline{C_L}$ show good convergence as P increases.

Meanwhile, the ratio of the grid size to the Kolmogorov length scale (Δ/η) is investigated here. The grid size, Δ, is determined based on the maximum dimension of a grid cell in all three directions, specifically $\Delta = \max(\Delta_x, \Delta_y, \Delta_z)$. The Kolmogorov length scale is calculated using the formula $\eta = (\nu^3/\varepsilon)^{1/4}$, where ε is the local dissipation rate. According to the findings of the studies by Moser & Moin (1987), Zhou *et al.* (2015), Zhou *et al.* (2019) and Mahmoodi-Jezeh & Wang (2020), it is crucial for the grid size to be of the same order as the Kolmogorov length scale, i.e. $O(\Delta/\eta) \sim O(1)$, to accurately capture the turbulence kinetic energy dissipation associated with the smallest scales of turbulence. The distribution of Δ/η for the typical case of $L/D = 5$ and $G/D = 0.3$ is illustrated in figure 2(*b*). The results show that Δ/η is generally less than 5, indicating that $\Delta/\eta = O(1)$. This confirms that the grid spacing is adequate for

https://doi.org/10.1017/jfm.2025.365 Published online by Cambridge University Press

P	N_v	N_d	N	$\overline{C_D}$	$\overline{C_L}$
4	19 658	3.02×10^7	96	0.63	0.74
5	19 658	4.72×10^7	96	0.61	0.76
6	19 658	6.79×10^7	96	0.61	0.76
7	19 658	9.25×10^7	96	0.62	0.76

Table 1. Time-averaged drag coefficient $\overline{C_D}$ and lift coefficient $\overline{C_L}$ of the rectangular cylinder with different orders of polynomial expansion P at $L/D = 5$ and $G/D = 0.3$. Here N_v is the number of elements, N_d is approximate degree of freedom and N is the number of Fourier planes.

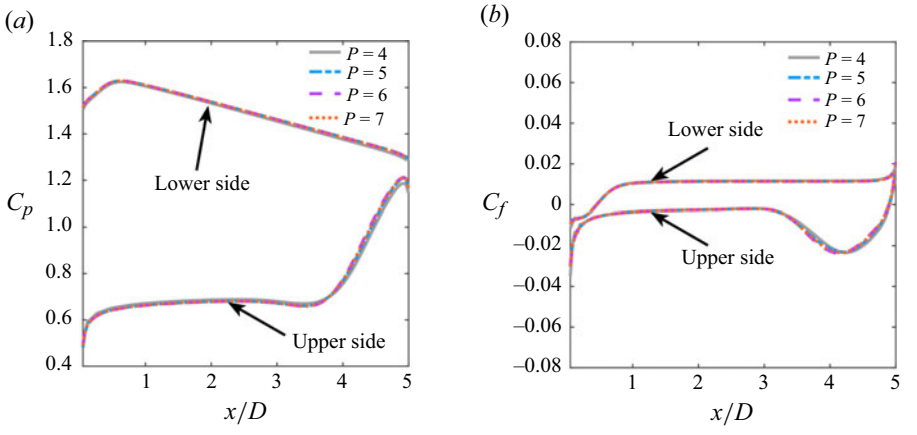


Figure 3. The time- and spanwise-averaged pressure coefficient profiles C_p (a) and skin friction coefficient profiles C_f (b) on the surface of the rectangular cylinder for various values of P at $L/D = 5$, $G/D = 0.3$.

accurately performing DNS of turbulent flows. Furthermore, the time- and spanwise-averaged pressure coefficient C_p and skin friction coefficient C_f on the surface of a rectangular cylinder are investigated, which are given by

$$C_p = \frac{\bar{p} - \bar{p}_{ref}}{0.5\rho U_0^2}, \quad C_f = \frac{\tau_w}{0.5\rho U_0^2}, \tag{2.3}$$

where $\bar{p}$ and $\bar{p}_{ref}$ are the mean surface pressure and the reference pressure, respectively, and τ_w is the mean shear stress. The profiles of C_p and C_f for various values of P at $L/D = 5$, $G/D = 0.3$ are shown figures 3(a) and 3(b), respectively. It can be observed that for different values of P, the C_p and C_f profiles on the lower surface of the rectangular cylinder nearly coincide. However, on the upper surface, both C_p and C_f are influenced by variations in P. Beyond for $x/D > 3.5$, the C_p and C_f at $P = 4$ exhibit a slight deviation from the other values of P for $x/D > 3.5$. In contrast, for $P \geqslant 5$, the C_p and C_f curves almost entirely overlap, indicating a stronger convergence. Thus, it is concluded that $P = 5$ and $N = 96$ are sufficient for the current simulations.

Once the flow reaches a statistically steady state, statistical data are accumulated at each time step throughout the simulation for further $200D/U_0$, and the sampling interval for the instantaneous 3-D flow field is set to $0.25D/U_0$, which also defines the time interval for signal sampling at the spatial points (Li *et al.* 2024*b*).

https://doi.org/10.1017/jfm.2025.365 Published online by Cambridge University Press

2.2. *Data analysis techniques*

2.2.1. *Visualization of Lagrangian coherent structures*

The finite-time Lyapunov exponents (FTLEs) method (Haller & Yuan 2000; Haller 2001; Shadden, Dabiri & Marsden 2006; Green, Rowley & Haller 2007; Shadden, Astorino & Gerbeau 2010; He *et al.* 2017; Wang *et al.* 2017, 2018; Wang & Wang 2021*a*; Li *et al.* 2024*b*) and virtual dye visualization (He *et al.* 2016; Wang & Wang 2021*b*; Cheng *et al.* 2022; Dong *et al.* 2024) serve as powerful tools for effectively tracking Lagrangian coherent structures (LCSs) in complex flows. Specifically, the flow map is defined as $\boldsymbol{\Phi}_{t_0}^{t_0+t_\Delta} : \mathbf{x}(t_0) \longrightarrow \mathbf{x}(t_0 + t_\Delta)$, which describes the mapping of fluid particles from their initial position $\mathbf{x}(t_0)$ at time t_0 to their new position $\mathbf{x}(t_0 + t_\Delta)$ at $t_0 + t_\Delta$. The FTLE at t_0 can be calculated as follows:

$$\sigma(\mathbf{x}, t_0, t_\Delta) = \frac{1}{|2t_\Delta|} ln \left(\lambda_{max} \left\{ \left[\frac{\partial \mathbf{x}(t_0 + t_\Delta)}{\partial \mathbf{x}(t_0)} \right]^T \left[\frac{\partial \mathbf{x}(t_0 + t_\Delta)}{\partial \mathbf{x}(t_0)} \right] \right\} \right). \tag{2.4}$$

In this context, $\sigma(\mathbf{x}, t_0, t_\Delta)$ represents the exponential growth rate of nearby trajectories over a finite time interval t_Δ, while $\lambda_{\max}$ denotes the largest singular value of the deformation gradient matrix. The integration can be conducted forward ($t_\Delta > 0$) or backward ($t_\Delta < 0$), resulting in FTLE ridges that exhibit repelling or attracting properties, respectively. The attracting property is employed for the extraction of LCSs, whereas the repelling property is utilized for virtual dye visualization.

2.2.2. *Dynamic mode decomposition analyses*

Dynamic mode decomposition (DMD) (Schmid 2010) is a significant modal analysis tool that has been widely utilized in previous studies (He *et al.* 2013*b*; Pan *et al.* 2017; Li *et al.* 2022*a*; Liu *et al.* 2022; Li *et al.* 2024*b*). The DMD effectively extracts a set of modes from the original unsteady dynamic flow, with each mode corresponding to spatial structures in the flow field that are dominant at a specific frequency. Therefore, in this work, DMD will be applied to extract the dominant frequency modes from the flow field snapshots, allowing for a comprehensive understanding of the underlying dynamics. The snapshots of the flow fields can be decomposed as follows:

$$\Phi(\mathbf{x}, t) = \mathbf{U}(\mathbf{x}) + \sum_{k=1}^{r} b_k \phi_k(\mathbf{x}) e^{\omega_k t}, \tag{2.5}$$

where Φ represents the reconstructed field and $\mathbf{U}$ denotes the mean field. The terms ϕ_k and b_k correspond to the kth DMD mode and its associated magnitude, respectively. In the present study, the DMD analysis is conducted on 3-D flow fields, with each sample consisting of the three velocity components.

3. Results and discussion

3.1. *Instantaneous 3-D vortices and statistics characteristics*

In this section, the visualization of instantaneous vortical structures are presented first. Then, this section examines the effects of the aspect ratio L/D and the gap ratio G/D on the mean flow statistics, specifically focusing on the mean field topology, the scales of separation bubbles, and fluctuations. These characteristics will provide a comprehensive overview of vortex generation and evolution in the FNRC and will serve as a basis for analysing the near-wall effects on vortex dynamics in § 3.2.

https://doi.org/10.1017/jfm.2025.365 Published online by Cambridge University Press

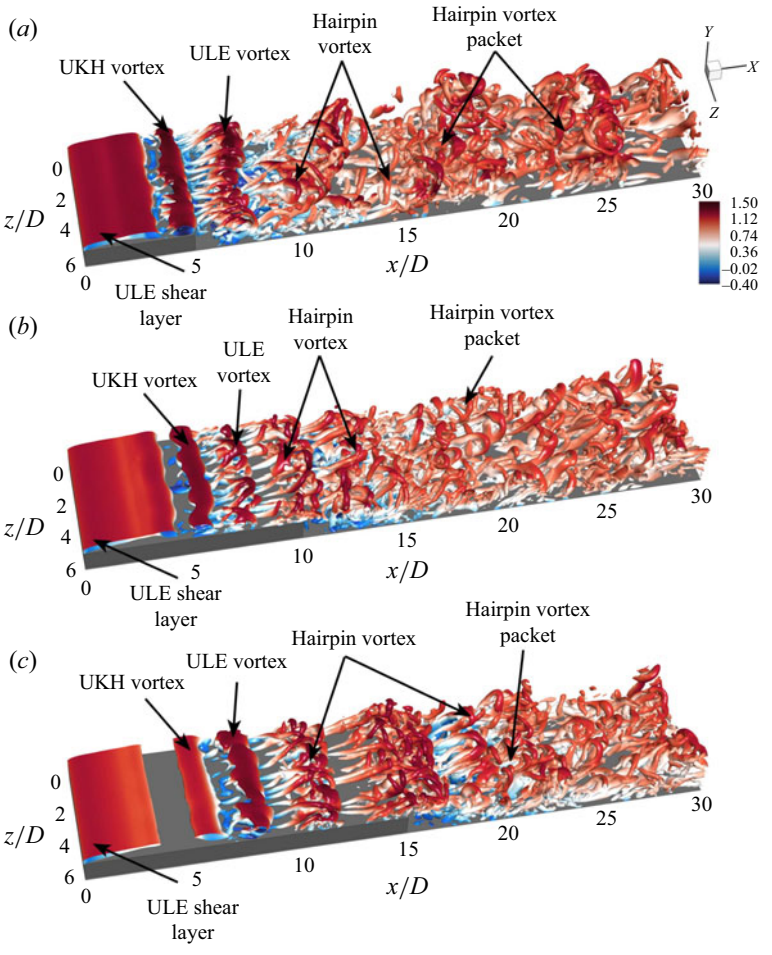


Figure 4. Instantaneous 3-D vortical structures visualized by isosurfaces of $Q = 0.1$ at $G/D = 0.1$, coloured with the instantaneous streamwise velocity u/U_0: (*a*) $L/D = 5$; (*b*) $L/D = 10$; (*c*) $L/D = 15$.

3.1.1. *Instantaneous 3-D vortex structures*

The instantaneous 3-D vortex structures for all flows are identified by the criterion with $Q = 0.1$. Figure 4 illustrates the instantaneous vortices for $G/D = 0.1$. The FNRC exhibits distinct asymmetry compared with the FIRC (Zhang *et al.* 2023; Li *et al.* 2024*b*) and aligns more closely with the FNCC (Li *et al.* 2022*a*) with the same G/D, featuring a turbulent boundary layer downstream rather than the wake of an isolated blunt body. The KH instability in the upper leading edge (ULE) shear layer results in the formation of a two-dimensional upper KH (UKH) vortex. The LE/TE shear layer is the structure that detaches from the LE/TE corner (Cimarelli *et al.* 2018*b*; Chiarini *et al.* 2021; Cimarelli *et al.* 2024; Li *et al.* 2024*b*). Moreover, there is no flow separation at the lower leading edge (LLE), leading to the absence of the vortices in the gap. As illustrated in figure 4(*a*), for $L/D = 5$ and $G/D = 0.1$, the near-wall effect causes the UKH vortices to form and merge farther downstream compared with the FIRC (Zhang *et al.* 2023; Li *et al.* 2024*b*), resulting in a larger streamwise scale of the mean LLE recirculation (shown in § 3.1.2). The 3-D instability of the ULE vortex manifests downstream of the UTE, rather than on the upper side of the rectangular cylinder, highlighting a significant contrast with

https://doi.org/10.1017/jfm.2025.365 Published online by Cambridge University Press

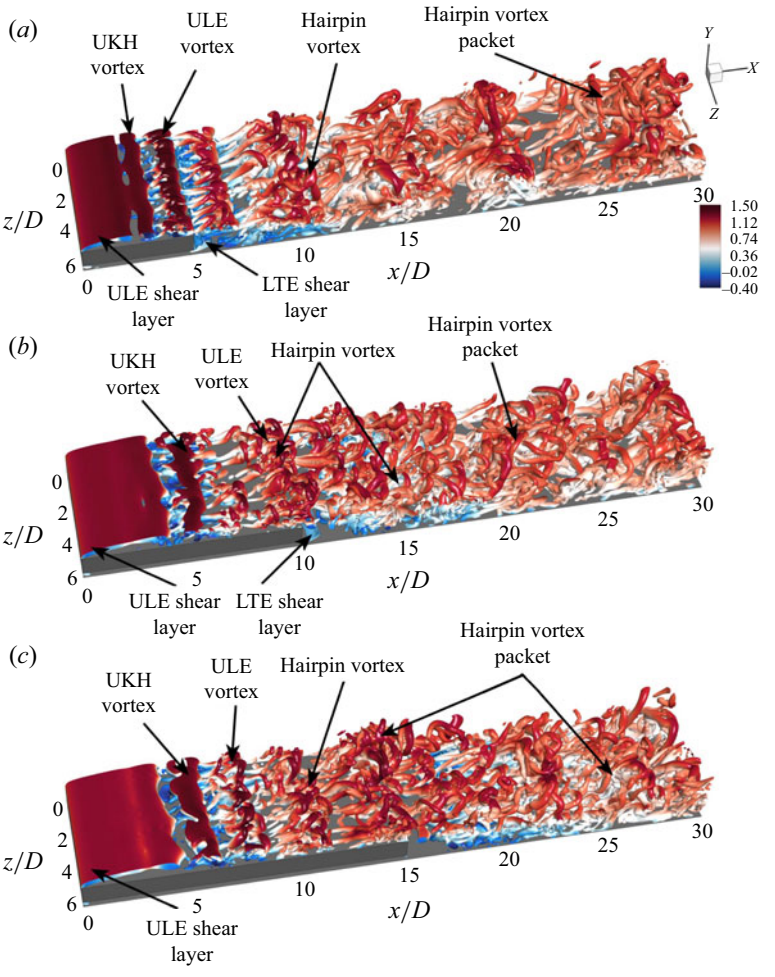


Figure 5. Instantaneous 3-D vortical structures visualized by isosurfaces of $Q = 0.1$ at $G/D = 0.3$, coloured with the instantaneous streamwise velocity u/U_0: (*a*) $L/D = 5$; (*b*) $L/D = 10$; (*c*) $L/D = 15$.

the flow characteristics observed in the FIRC (Zhang *et al.* 2023; Li *et al.* 2024*b*). As the ULE vortices interact with the downstream reverse wall boundary layer, hairpin vortices eventually form. For $L/D = 10$ and 15, as shown in figures 4(*b*) and 4(*c*), the UKH vortices interact with the reverse boundary layer on the upper cylinder surface, evolving into hairpin vortices. For all these three flows, upon reattachment to the plate, the flow transitions into a wall boundary layer, with hairpin vortex packets forming farther downstream.

For $G/D = 0.3$, the instantaneous 3-D vortical structures are shown in figure 5. The KH instability in the ULE shear layer is observed across all three flows, leading to the formation of KH vortices. The absence of vortical structures within the gap indicates significant suppression of the LLE shear layer. In contrast to $G/D = 0.1$, the lower trailing edge (LTE) shear layer extends from the LTE for $L/D = 5$ and $L/D = 10$ (in figure 5*a* and 5*b*). However, at $L/D = 15$, the LTE shear layer is negligible, as shown in figure 5(*c*). At $L/D = 5$, as shown in figure 5(*a*), the UKH vortex forms farther downstream on the upper side of the cylinder. Consequently, the merged UKH vortex undergoes 3-D

https://doi.org/10.1017/jfm.2025.365 Published online by Cambridge University Press

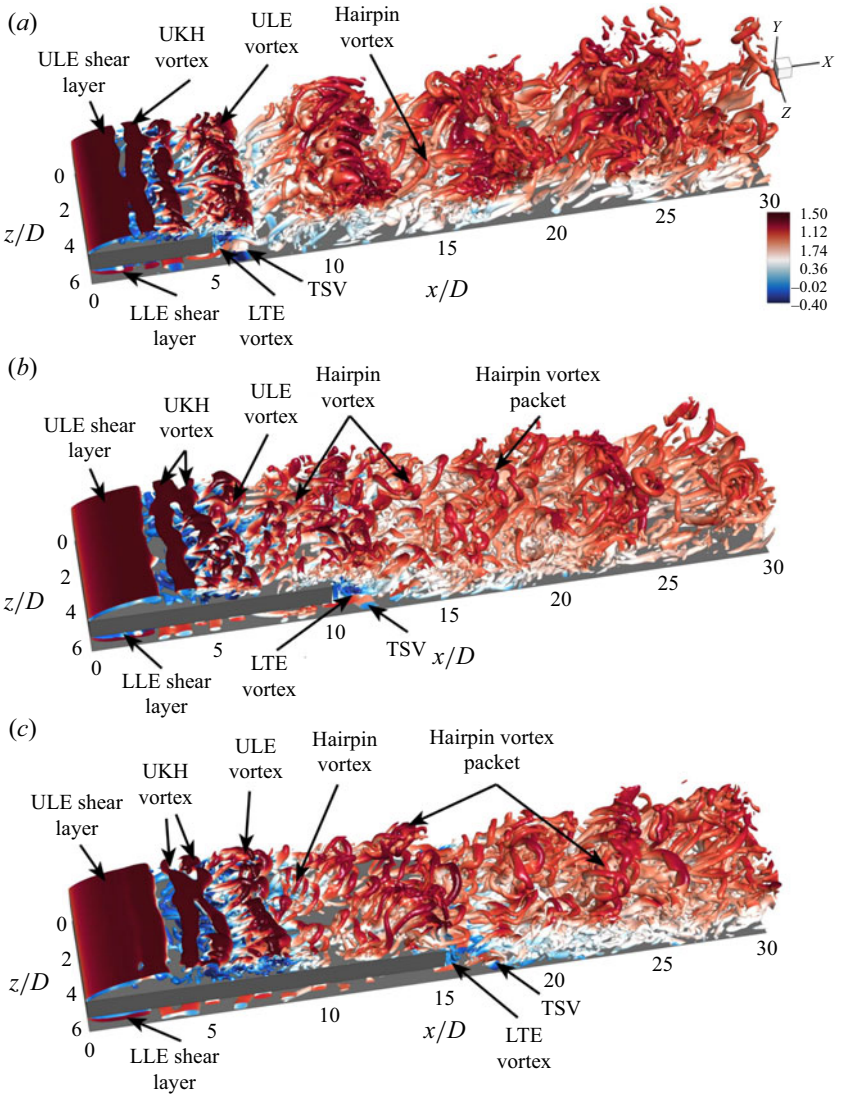


Figure 6. Instantaneous 3-D vortical structures visualized by isosurfaces of $Q = 0.1$ at $G/D = 0.9$, coloured with the instantaneous streamwise velocity u/U_0: (*a*) $L/D = 5$; (*b*) $L/D = 10$; (*c*) $L/D = 15$.

instability and evolves into the ULE vortex downstream. No hairpin vortices are present on the upper side, similar to the flow at $G/D = 0.1$. However, at $L/D = 10$ and 15 (in figure 5*b* and *c*), hairpin vortex packets appear on the upper side, which contrasts with the flow at $G/D = 0.1$. Furthermore, the distribution of ULE vortices becomes more intricate. When the gap ratio increases to $G/D = 0.9$, as shown in figure 6, the influence of the upstream wall boundary layer diminishes, leading to the formation of a distinct LLE shear layer. In the gap, vortices are observed across all three L/D configurations, indicating that KH vortices shed from the LLE shear layer, unlike at $G/D = 0.1$ and 0.3. Both the LTE and TSVs are identifiable and closely related to the LLE vortex. The complexity of the vortical structures on the upper side of the cylinder increases.

https://doi.org/10.1017/jfm.2025.365 Published online by Cambridge University Press

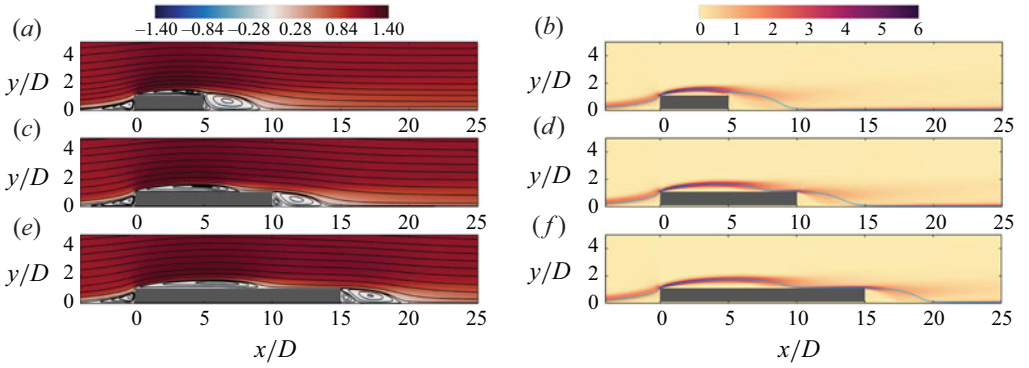


Figure 7. Time- and spanwise-averaged streamwise velocity U/U_0 in pseudocolour with the superimposition of streamlines for $G/D = 0.1$: (*a*) $L/D = 5$; (*c*) $L/D = 10$; (*e*) $L/D = 15$. The principal stretching σ_1 for $G/D = 0.1$: (*b*) $L/D = 5$; (*d*) $L/D = 10$; (*f*) $L/D = 15$. The cures in (*b*), (*d*) and (*f*) are the local streamlines.

3.1.2. *Mean flow characteristics*

The presence of a strong shear layer induced by the plate wall results in pronounced mean shear characteristics near the rectangular cylinder. Consequently, an investigation of these mean shear characteristics is undertaken in this section. Exploiting the spanwise homogeneity, the mean shear tensor in the $x-y$ plane is decomposed, which provides a comprehensive assessment of all non-zero components of the 3-D mean strain rate tensor (S_{xy}) (Fang & Tachie 2020),

$$S_{xy} = \begin{bmatrix} \dfrac{\partial U}{\partial x} & \dfrac{1}{2}\left(\dfrac{\partial U}{\partial y} + \dfrac{\partial V}{\partial x}\right) \\ \dfrac{1}{2}\left(\dfrac{\partial U}{\partial y} + \dfrac{\partial V}{\partial x}\right) & \dfrac{\partial V}{\partial y} \end{bmatrix} = \mathbf{M} \begin{bmatrix} \sigma_1 & 0 \\ 0 & \sigma_2 \end{bmatrix} \mathbf{M}^T, \tag{3.1}$$

where σ_1 and σ_2 are eigenvalues of S_{xy}, while $\mathbf{M}$ denotes the matrix of eigenvectors of S_{xy}. Due to the incompressibility and the spanwise homogeneity of the mean flow, it follows that $\sigma_1 + \sigma_2 = \partial U/\partial x + \partial V/\partial y = 0$. Consequently, it can be inferred that $\sigma_1 = -\sigma_2$, with σ_1 defined as positive to represent the magnitude of principal stretching. The time- and spanwise-averaged streamwise velocity (U/U_0) fields for different cases are presented in figures 7(*a*, *c*, *e*)–9(*a*, *c*, *e*). Meanwhile, the fields of principal stretching σ_1, which reflect the distribution of mean shear strength, are displayed in figures 7(*b*, *d*, *f*)–9(*b*, *d*, *f*).

For $G/D = 0.1$, a recirculation zone forms upstream of the rectangular cylinder in all flow cases, as shown in figure 7(*a*, *c*, *e*). The streamwise scale of this recirculation, which exceeds $3.7D$ for all three flows, is significantly larger than the scale observed in the FNCC, where it is smaller than $2D$ (Li *et al.* 2022*b*). This scale can be determined by the location of the reattachment point of the recirculation. On the upper side of the cylinder, a LE recirculation forms, similar to the FIRC (Zhang *et al.* 2023; Li *et al.* 2024*b*), but with no recirculation on the lower side, creating an asymmetry not seen in the FIRC (Cimarelli *et al.* 2018*b*; Chiarini *et al.* 2022*a*; Li *et al.* 2022*a*; Zhang *et al.* 2023; Cimarelli *et al.* 2024). For $L/D = 5$, the LE recirculation nearly spans the entire upper surface of the cylinder without a distinct reattachment point, differing from the FIRC (Cimarelli *et al.* 2019*a*; Chiarini & Quadrio 2021; Chiarini *et al.* 2021; Zhang *et al.* 2023; Li *et al.* 2024*b*). Immediately downstream of the cylinder, only a LTE recirculation is observed, with a significant wall recirculation also present, similar to the FNCC (He *et al.* 2013*a*,*b*, 2017;

https://doi.org/10.1017/jfm.2025.365 Published online by Cambridge University Press

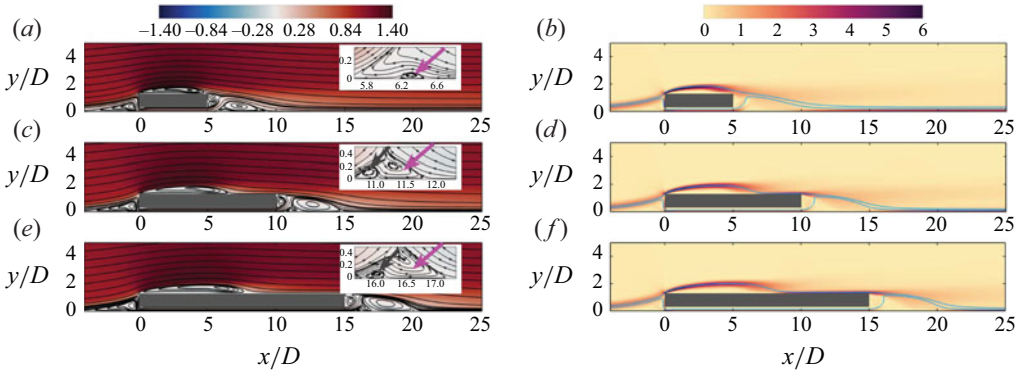


Figure 8. Time- and spanwise-averaged streamwise velocity U/U_0 in pseudocolour with the superimposition of streamlines for $G/D = 0.3$: (*a*) $L/D = 5$; (*c*) $L/D = 10$; (*e*) $L/D = 15$. The insets in (*a*), (*c*) and (*e*) are the close-up views. The black arrow marks the clockwise recirculation, while the magenta ones mark the anticlockwise recirculation. The principal stretching σ_1 for $G/D = 0.3$: (*b*) $L/D = 5$; (*d*) $L/D = 10$; (*f*) $L/D = 15$. The cures in (*b*), (*d*) and (*f*) are the local streamlines.

Li *et al.* 2022*b*), but with a smaller streamwise scale across all L/D configurations. This difference arises because KH instability in the upper shear layer in the FNCC develops farther downstream (Li *et al.* 2022*a*). The distribution of recirculations resembles that in backward-facing step flows (Ma & Schröder 2017; Li *et al.* 2020; Ma, Tang & Jiang 2020), suggesting that the FNCC shear layer is more stable than the UTE shear layer in the current FNRC at the same G/D, mainly due to the absence of upstream vortex disturbances. At $L/D = 5$, the LE recirculation connects with the downstream wall recirculation, forming a continuous recirculation zone, allowing fluid to return from the downstream region to the upper side upstream of the cylinder. As shown in figure 7(*b*, *d*, *f*), the upstream wall boundary layer, ULE shear layer and UTE shear layer (for $L/D = 10$, 15) exhibit strong shear characteristics. The upstream wall boundary layer rises upon encountering the rectangular cylinder, contributing to the formation of the upstream recirculation.

As G/D increases to 0.3, the upstream recirculation persists, accompanied by the downstream wall recirculation, as illustrated in figure 8. The gap flow significantly enhances, obstructing the connection between the wall recirculation and the TE, in contrast to $G/D = 0.1$. For $L/D = 5$, the LE recirculation covers nearly the entire upper surface, with a distinct reattachment point and two recirculations behind the cylinder, differing from $G/D = 0.1$. For $L/D = 10$ and 15, only one LTE recirculation is observed, as depicted in figures 8(*c*) and 8(*e*). Compared with the FNCC (He *et al.* 2013*a*,*b*, 2017; Li *et al.* 2022*b*), a novel feature is the occurrence of multiple flow separations at the downstream wall recirculation, as seen in the insets of figure 8(*a*,*c*,*e*). At $L/D = 5$, only an anticlockwise recirculation is observed beneath the wall recirculation (marked by the magenta arrow). However, at $L/D = 10$ and 15, both anticlockwise (marked by the magenta arrow) and clockwise (marked by the black arrow) recirculations appear. The distributions of σ_1 in figure 8(*b*, *d*, *f*) are similar to those at $G/D = 0.1$, although the shear strength beneath the rectangular cylinder is slightly higher for all three cases at $G/D = 0.3$.

At $G/D = 0.9$, the upstream wall recirculation weakens, and the gap flow increases significantly, as shown in figure 9(*a*, *c*, *e*). Unlike at $G/D = 0.1$ and 0.3, a LLE recirculation forms, with both its streamwise and wall-normal scales smaller than those of the ULE recirculation, indicating the establishment of the LLE shear layer.

https://doi.org/10.1017/jfm.2025.365 Published online by Cambridge University Press

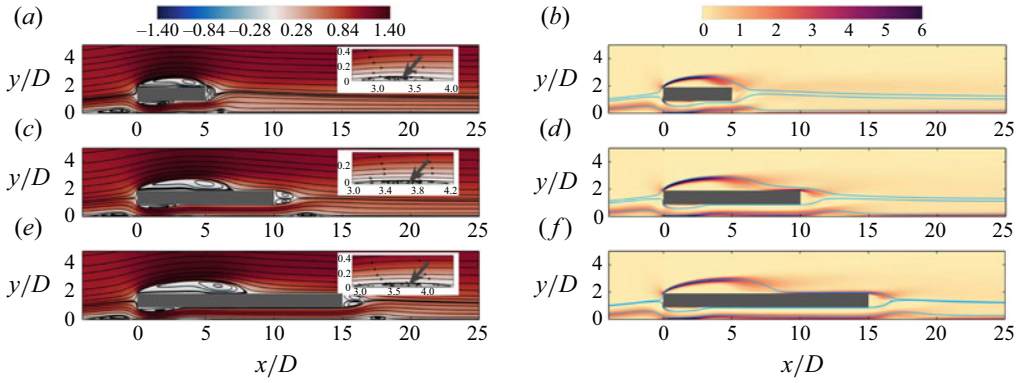


Figure 9. Time- and spanwise-averaged streamwise velocity U/U_0 in pseudocolour with the superimposition of streamlines for $G/D = 0.9$: (*a*) $L/D = 5$; (*c*) $L/D = 10$; (*e*) $L/D = 15$. The insets in (*a*), (*c*) and (*e*) are the close-up views. The black arrow marks the clockwise recirculation. The principal stretching σ_1 for $G/D = 0.9$: (*b*) $L/D = 5$; (*d*) $L/D = 10$; (*f*) $L/D = 15$. The cures in (*b*), (*d*) and (*f*) are the local streamlines.

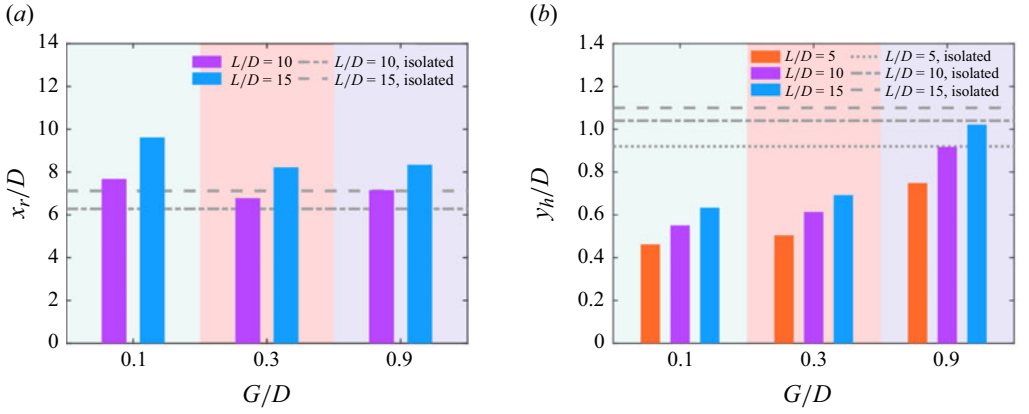


Figure 10. The quantified size of the ULE recirculation: (*a*) the streamwise scale x_r; and (*b*) wall-normal scale y_h, compared with these for the FIRC at the same Re (Li *et al.* 2024*b*), respectively.

The recirculation pair behind the cylinder, though not perfectly symmetrical, resembles that in the FIRC, with two distinct recirculations, signalling a diminished near-wall effect. As shown in figure 9(*b*, *d*, *f*), the upstream wall boundary layer lifting is reduced and no longer contacts the cylinder. Additionally, figure 9(*a*, *c*, *e*) show a small clockwise recirculation (marked by the black arrow) beneath the LLE recirculation, suggesting that the LLE vortex induces wall boundary layer separation. The downstream wall recirculation persists, indicating continued separation of the downstream wall boundary layer, but its scale is significantly reduced.

Figures 7 to 9 show that the size of the ULE recirculation changes with increasing G/D. The streamwise (x_r) and wall-normal (y_h) scales of the ULE recirculation are quantified in figures 10 (*a*) and 10(*b*), respectively, with comparison with the LE recirculation in the FIRC at the same Re. Here x_r is determined by the reattachment point, where the wall friction coefficient changes from a negative value to a positive value. Since the streamwise velocity is negative within the recirculation, y_h is determined by the point with the maximum wall-normal position within the recirculation. For $L/D = 5$, the ULE recirculation nearly covers the entire upper surface, resulting in a significantly larger x_r

https://doi.org/10.1017/jfm.2025.365 Published online by Cambridge University Press

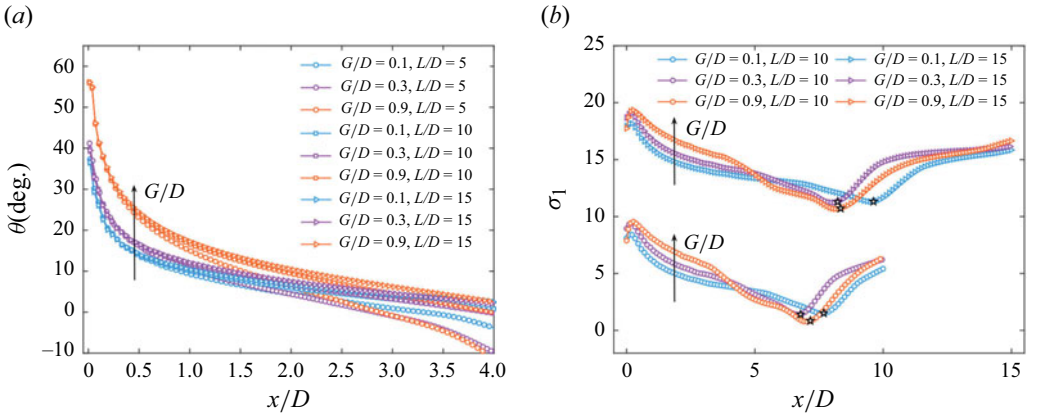


Figure 11. (*a*) The local angle θ between the ULE shear layer and the x coordinate. (*b*) The local principal stretching σ_1 along the ULE shear layer for $L/D = 10$ and 15. The values for $L/D = 15$ are increased by 10. The pentagrams represent the locations where the flows reattach.

compared with the FIRC (Li *et al.* 2024*b*). As shown in figure 10(*a*), the streamwise scale x_r for $L/D = 10$ and 15 is also larger than in the FIRC, indicating that the near-wall effect delays reattachment. In contrast, the wall-normal scale y_h, shown in figure 10(*b*), is smaller than in the FIRC (Li *et al.* 2024*b*). Notably, y_h increases with G/D, reflecting a reduced near-wall effect as G/D increases. Additionally, for the same G/D, a larger streamwise span of the cylinder results in a larger y_h for the ULE recirculation.

To understand the factors influencing the scale of the ULE recirculation, the local angle θ between the ULE shear layer and the x axis is calculated. The position of ULE shear layer is defined by the local mean streamline, as shown in figures 7 to 9. Figure 11(*a*) shows that the ULE shear layer initially deflects upward but this deflection decreases downstream. The initial deflection angle is nearly uniform for the same G/D, with minimal dependence on L/D. The mean shear resulting from the upstream wall boundary layer suppresses the wall-normal growth of the ULE recirculation. Therefore, smaller G/D corresponds to a smaller deflection angle, indicating a diminishing influence of the upstream wall boundary layer as G/D increases. This explains the increasing wall-normal scale of the ULE recirculation with higher G/D, as shown in figure 10(*b*). Figure 11(*b*) shows that the local principal stretching σ_1 for $L/D = 10$ and 15 behaves similarly across all cases. Initially, the mean shear increases to a maximum before decreasing to a minimum near the reattachment point. As the G/D increases, the initial principal stretching becomes more pronounced, while the decay occurs more steeply. A larger G/D also results in a larger y_h, and although the decay is most rapid when $G/D = 0.9$, the larger y_h causes the decay to reach its minimum at a more downstream location. In contrast, the flow with $G/D = 0.3$ reaches its minimum value and reattaches at a more upstream position, which explains the smaller streamwise scales of the ULE recirculation observed for $G/D = 0.3$, as shown in figure 10(*a*). The flow with $G/D = 0.1$, on the other hand, experiences the weakest decay, yet its wall-normal scale of the ULE recirculation is similar to that of the flow with $G/D = 0.3$. As a result, the flow with $G/D = 0.1$ ultimately decays to its minimum value, with reattachment occurring at the farthest downstream location.

To further illustrate these mean flow features, $U_{max} = \max_{y/D>1+G/D} U(x/D, y/D)$ is extracted and shown in figure 12 (*a*). Here U_{max} represents the flow velocity along the ULE shear layer (Chiarini & Auteri 2023). By examining figures 11(*a*) and 12(*a*) together, it is evident that as the streamline passes over the upper LE corner, the curvature increases,

https://doi.org/10.1017/jfm.2025.365 Published online by Cambridge University Press

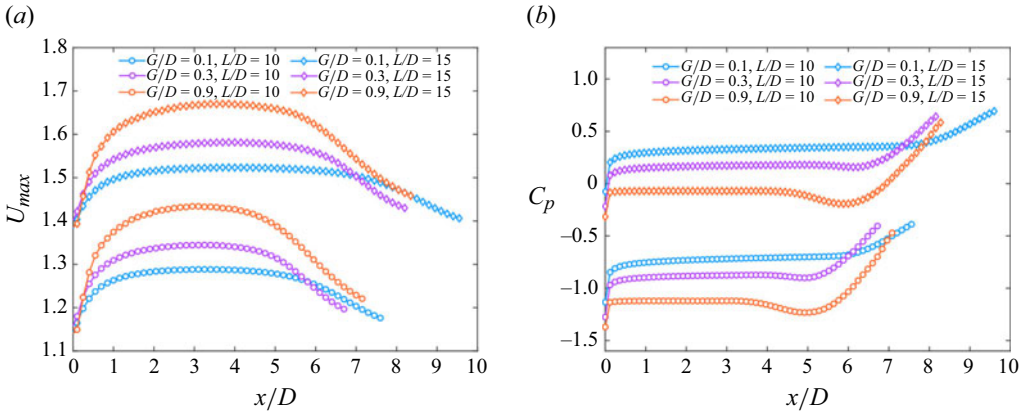


Figure 12. (*a*) The maximum mean streamwise velocity, U_{max}, over the upper surface of the cylinder at a given x position, where $x/D = 0 \sim x_r/D$. The values for $L/D = 15$ are increased by 0.25. (*b*) The mean pressure coefficient C_p, referring to the free stream pressure, along the upper LE shear layer. The values for $L/D = 15$ are increased by 1.

resulting in a higher flow acceleration. This observation aligns with the findings in the study of Chiarini & Auteri (2023). Meanwhile, in the current study, an increase in G/D results in greater flow acceleration for the same L/D. As a result, U_{max} increases with an increase in G/D. It should be noted that this trend contrasts with the findings of Chiarini & Auteri (2023), who explores the FNRC with low Re and a moving wall. This difference is likely driven by Re, as the LE flow separation in the FIRC exhibits distinct behaviour at current moderate Re (Zhang *et al.* 2023; Li *et al.* 2024*b*) compared with lower Re (Chiarini *et al.* 2021). Additionally, the effect of the incoming boundary layer is significant, especially for small G/D. However, to a significant extent, this observation helps clarify why an increase in G/D leads to a larger y_h, giving that the flow velocity decreases as one approaches the wall. After undergoing an approximate plateau, U_{max} gradually decreases, signalling that the flow is nearing reattachment. The attenuation of velocity is closely linked to local pressure variations. As shown in figure 12(*b*), the flow experiences a reversed pressure gradient prior to reattachment. Furthermore, for the same L/D, the larger G/D, the greater the reversed pressure gradient. However, similar to the decay of σ_1, although the reversed pressure gradient at $G/D = 0.9$ is stronger than at $G/D = 0.3$, the flow at $G/D = 0.9$ has a larger U_{max}, resulting in a longer decay process. Ultimately, the flow at $G/D = 0.3$ decays to its minimum value at the closest point, while the flow at $G/D = 0.1$ decays at the furthest point, due to its significantly smaller reversed pressure gradient and the fact that the reversed pressure gradient appears at a later location.

The spanwise-averaged root-mean-square (r.m.s) of the streamwise velocity fluctuation, u'_{rms}/U_0, is shown in figure 13. The fluctuations near the LE are relatively weak, suggesting laminar flow characteristics. However, as the KH vortices develop, there is a substantial increase in the velocity fluctuations. At $G/D = 0.1$ and 0.3 (in figures 13*a* and 13*b*), the distributions of u'_{rms}/U_0 are similar. Strong fluctuations occur primarily on the upper side of the cylinder and downstream, with negligible fluctuations below it, indicating that the LLE and LTE shear layers are very weak at these smaller G/D values. When G/D increases to 0.9 (in figure 13*c*), fluctuations extend from the LLE, although they are weaker than those on the upper side. Weak fluctuations also appear beneath the cylinder on the plate wall. This behaviour aligns with the mean streamwise velocity distribution (in figure 9), where the LLE shear layer forms, separates and induces the separation of the wall boundary layer. Distinct fluctuations also extend from the LTE, indicating alternative TE

https://doi.org/10.1017/jfm.2025.365 Published online by Cambridge University Press

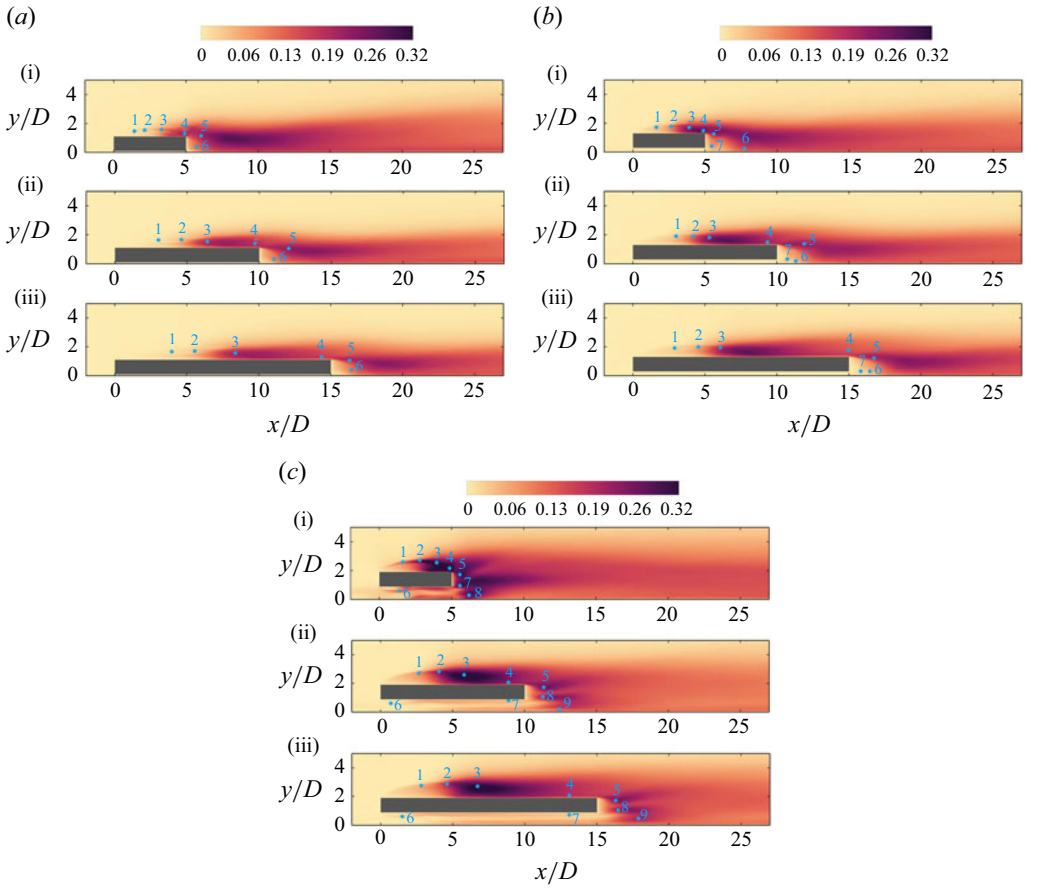


Figure 13. The spanwise-averaged the r.m.s. of the streamwise fluctuations u'_{rms}/U_0:(*a*) $G/D = 0.1$; (*b*) $G/D = 0.3$; (*c*) $G/D = 0.9$; (i) $L/D = 5$; (ii) $L/D = 10$; (iii) $L/D = 15$. The fluctuations from these azure points are extracted to calculate the local power spectral densities (PSDs).

vortex shedding and contributing to the separation of the plate wall boundary layer near the LTE. Overall, as the cylinder moves away from the wall, fluctuations gradually increase, suggesting that the near-wall effect on vortex generation and evolution diminishes with increasing G/D.

3.2. *Crucial intricacies of vortex dynamics*

The evolution of instantaneous vortex structures is a crucial aspect of vortex dynamics. Accordingly, this section presents an analysis of the near-wall effect on the instantaneous vortical characteristics.

The dynamics of the downstream recirculation at $L/D = 5$ are explored, focusing on the merging of the ULE and downstream recirculations observed in the mean flow at $L/D = 5$ and $G/D = 0.1$, as illustrated in figure 7(*a*). Instantaneous characteristics of the downstream wall recirculation are examined using the virtual dye visualization technique, with comparisons made for $G/D = 0.3$ and 0.9. The position of the virtual dye release is determined by the location of the mean downstream wall recirculation. The initial streamwise positions of the virtual dyes are set at the centre of the recirculation, spanning a range of $0.25D$. Their wall-normal positions are fixed at $0.05D$, with the dyes being

https://doi.org/10.1017/jfm.2025.365 Published online by Cambridge University Press

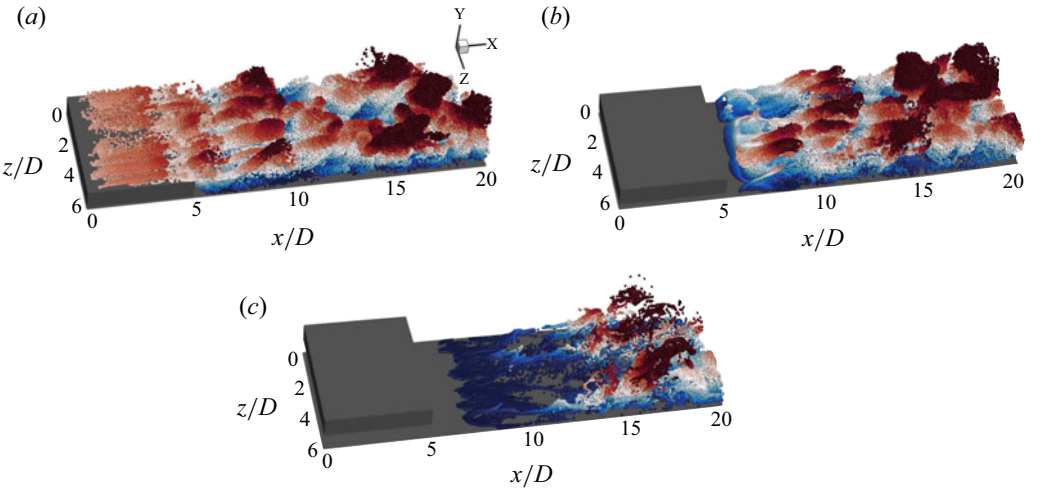


Figure 14. Results of tracking the evolution of the downstream wall recirculation at $L/D = 5$ for different G/D, revisited by virtual dye visualization: (*a*) $G/D = 0.1$; (*b*) $G/D = 0.3$; (*c*) $G/D = 0.9$. Colours represent wall-normal heights: red for higher heights and blue for lower heights.

uniformly distributed along the spanwise direction. Their spatial distributions, shown in figure 14, reveal that significant amounts of dye migrate to the upper side of the cylinder at $G/D = 0.1$ (in figure 14*a*). In contrast, for $G/D = 0.3$ and 0.9, no dye is present above the cylinder (in figures 14*b* and 14*c*), indicating that at $G/D = 0.1$, downstream fluid is transported to the upper side of the cylinder due to wall recirculation. The distribution of virtual dyes in the near wake region shows the highest concentration for $G/D = 0.1$ and the lowest for $G/D = 0.9$, consistent with the mean flow, where larger G/D values result in weaker separation of the downstream wall boundary layer.

3.2.1. *The $G/D = 0.1$ cases*

The vortex distribution on the upper side of the cylinder at $L/D = 5$ and $G/D = 0.1$ differs significantly from the FIRC at the same *Re* (Zhang *et al.* 2023; Li *et al.* 2024*b*) (in figure 4), necessitating a detailed examination of the vortex dynamics, particularly the formation of the ULE vortex. The evolution of the vortex dynamics is shown in figure 15(*a*, *b*), with the instantaneous pressure distribution at $z/D = \pi$ in figure 15(*c*, *d*). At $t = t_0$, a merged UKH vortex forms near the UTE (in figure 15*a*), creating a low-pressure region and inducing a reverse flow beneath it, as seen in figure 15(*c*). Meanwhile, the UKH vortex undergoes 3-D instability and evolving into the ULE vortex. This reverse flow, encountering an adverse pressure gradient (in the inset of figure 15*c*), causes the separation of the upper boundary layer, forming an anticlockwise-rotating SV on the upper side of the cylinder (USV), marked by the magenta arrow in figure 15(*a*). This USV is absent in the FIRC (Zhang *et al.* 2023; Li *et al.* 2024*b*). The upstream motion generated by the downstream wall recirculation enhances the local reverse flow, which is a key factor contributing to the generation of the USV. At $t = t_0 + 12\Delta t$ (in figures 15*b* and 15*d*), the ULE vortex detaches from the cylinder, displaying strong 3-D features and interacting with the wall recirculation. While the initial USV disappears, a new one forms due to the induction of the newly generated UKH vortex. The wall recirculation induced by the new UKH vortex passes over the UTE (in figure 15*b*). This interaction directly contributes to the integration of the ULE recirculation and the downstream wall recirculation in the

https://doi.org/10.1017/jfm.2025.365 Published online by Cambridge University Press

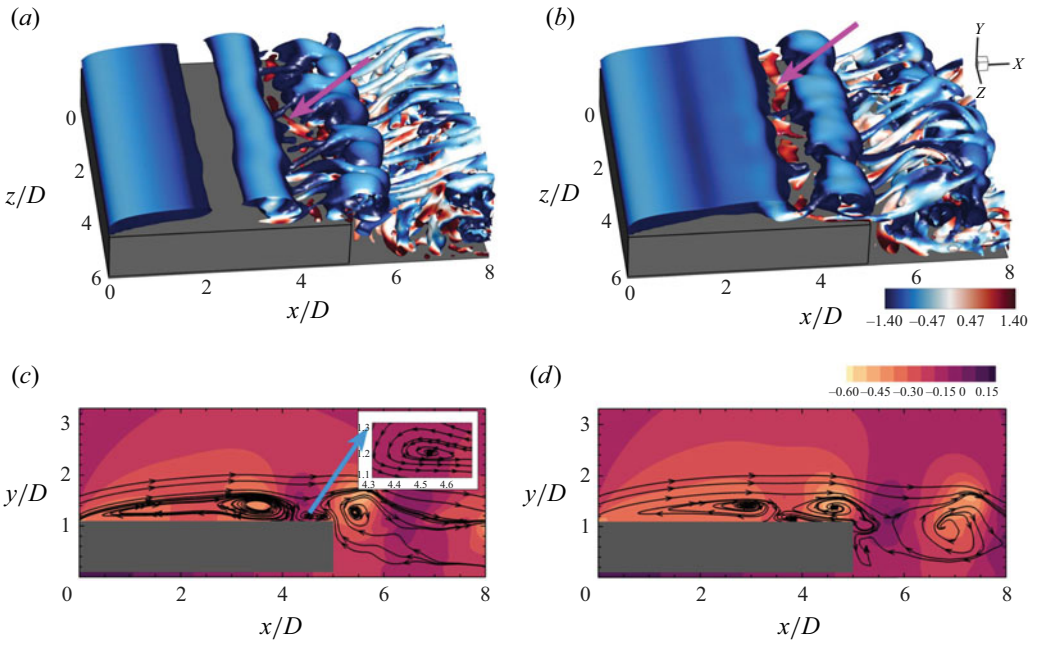


Figure 15. (*a,b*) The process of the LLE vortex developing from the UKH vortex at $L/D = 5$ and $G/D = 0.1$. (*c,d*) The corresponding instantaneous distribution of the pressure with the superimposition of instantaneous streamlines at $z/D = \pi$. Here (*a,c*) $t = t_0$; (*b,d*) $t = t_0 + 12\Delta t$, where $\Delta t = 0.25D/U_0$. The vortical structures are visualized by isosurfaces of $Q = 0.1$, coloured with the instantaneous spanwise vorticity ω_z. The magenta arrow in (*a*) and (*b*) marks the SV with positive ω_z on the upper side of the cylinder. The insets in (*c*) are the close-up views.

mean field (in figure 7*a*) and prevents the formation of UTE vortices in the current flow. To confirm this phenomenon, 3-D FTLEs are employed.

As shown in figure 16(*a*, *b*), the UKH vortex evolves into the ULE vortices as it passes over the UTE, but no UTE vortex is formed during this process. This confirms that UTE vortices do not form for $L/D = 5$ and $G/D = 0.1$. While the reverse uplift of the downstream wall recirculation is observed. The formation of UTE vortices at larger aspect ratios is also examined. For $L/D = 15$, the flow characteristics are similar to those for $L/D = 10$. Therefore, only the vortex dynamics near the UTE for $L/D = 10$ are shown in figure 16(*c*, *d*). At time $t = t_0$ (in figure 16*c*), the ULE vortex forms a hairpin vortex near the UTE, while the UTE shear layer rolls up, initiating the formation of a UTE vortex. This formation is driven by the KH instability of the UTE shear layer, similar to backward-facing step flows (Ma & Schröder 2017; Li *et al.* 2020; Ma *et al.* 2020). By $t = t_0 + 4\Delta t$ (in figure 16*d*), the UTE vortex fragments due to interactions with the wall recirculation, and is entrained into the wake and dissipates. In contrast, the ULE vortex retains its hairpin vortex shape and continues to evolve downstream, becoming the dominant feature in the plate boundary layer.

3.2.2. *The $G/D = 0.3$ cases*

To examine the development of the UTE and LTE shear layers at $G/D = 0.3$, FTLEs are also used for visualization. The evolution for $L/D = 5$ is illustrated in figure 17(*a*, *b*). At $t = t_0$ (in figure 17*a*), the UTE shear layer rolls up, forming the UTE vortex. This process contrasts with the flow at $G/D = 0.1$ for the same L/D. Moreover, the UTE shear layer deflects downwards, contributing to the formation of an upper recirculation

https://doi.org/10.1017/jfm.2025.365 Published online by Cambridge University Press

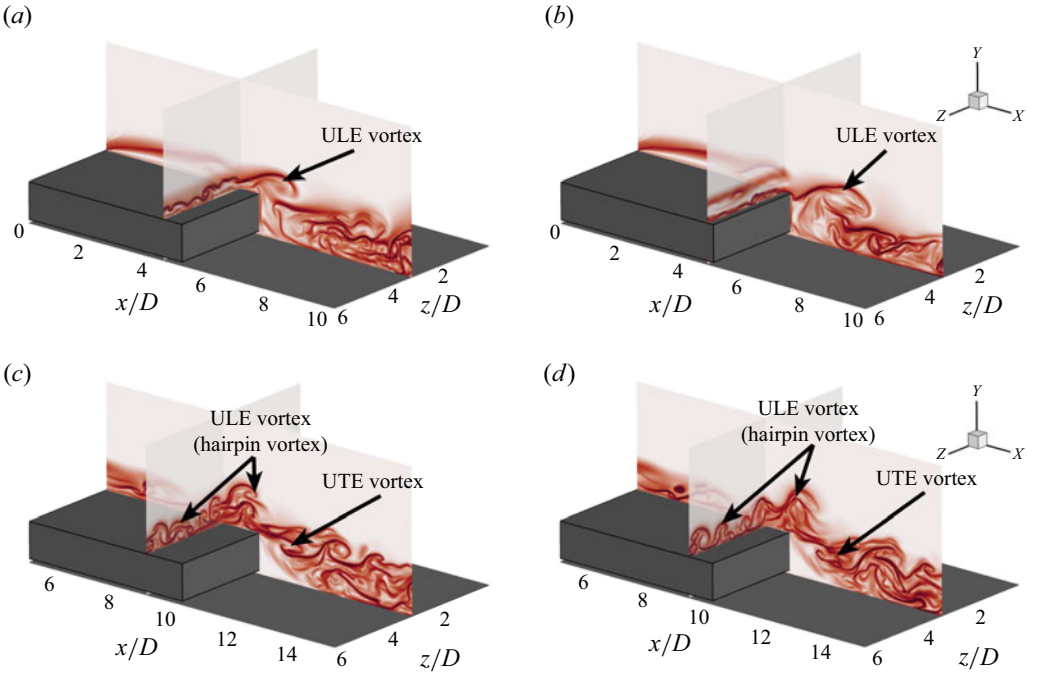


Figure 16. The vortex evolution process revealed by LCSs presented in the slices at $G/D = 0.1$: (*a,b*) the ULE vortex for $L/D = 5$, (*c,d*) the UTE vortex for $L/D = 10$. Here (*b*) and (*d*) are delayed by $8\Delta t$ and $4\Delta t$ compared with (*a*) and (*c*), respectively, where $\Delta t = 0.25D/U_0$.

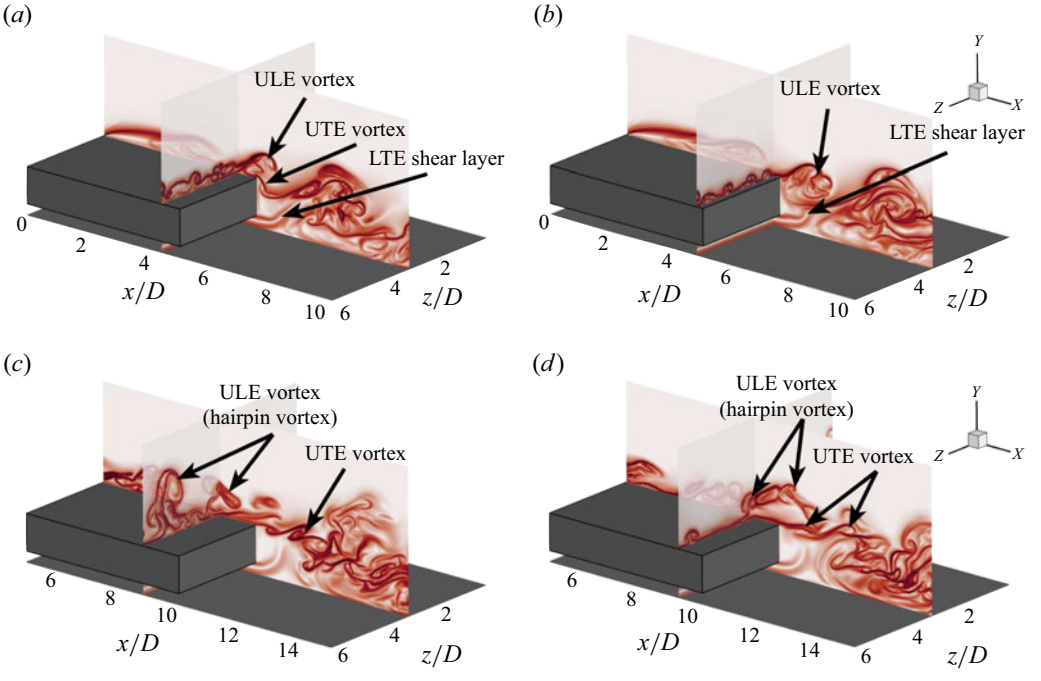


Figure 17. The evolution process of the UTE vortex revealed by LCSs presented in the slices at $G/D = 0.3$: (*a,b*) $L/D = 5$; (*c, d*) $L/D = 10$. Here (*b*) and (*d*) are delayed by $6\Delta t$ and $8\Delta t$ compared with (*a*) and (*c*), respectively, where $\Delta t = 0.25D/U_0$.

https://doi.org/10.1017/jfm.2025.365 Published online by Cambridge University Press

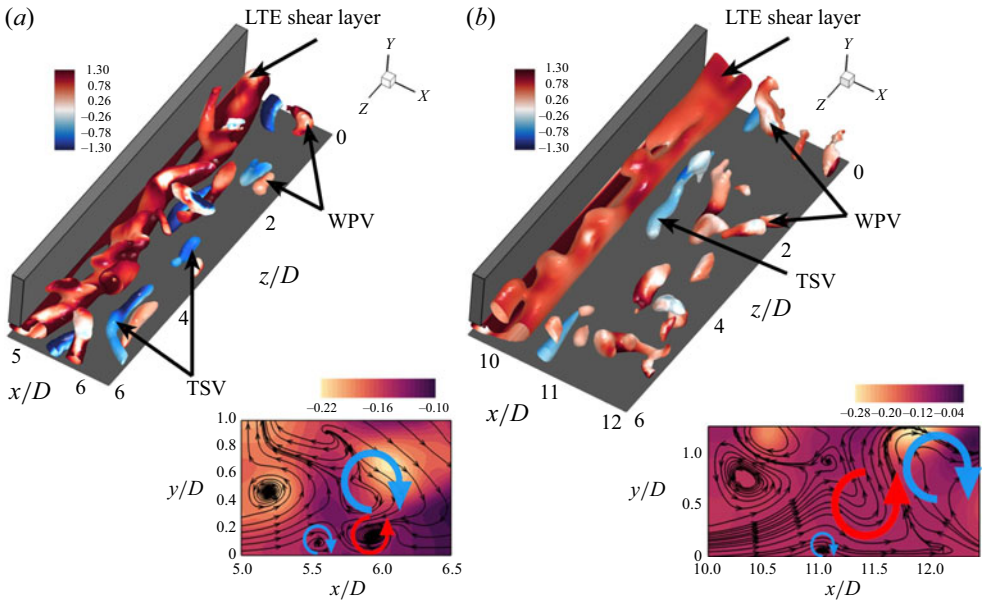


Figure 18. Close-up view of the instantaneous SV near the TE (TSV) and the vortex with positive spanwise vorticity on the plate wall (WPV) at $G/D = 0.3$, visualized by isosurfaces of $Q = 0.05$ and coloured with the instantaneous spanwise vorticity ω_z, along with the slices showing the contours of instantaneous pressure with the superimposition of streamlines at $z/D = 0$: (*a*) $L/D = 5$;(*b*) $L/D = 10$. The azure rotation arrow represents local clockwise motion; the red rotation arrow represents local anticlockwise motion.

(in figure 8*a*). As the flow progresses, the UTE vortex is entrained into the wake and disappears (in figure 17*b*). Meanwhile, the LTE shear layer lifts but does not roll up, preventing the formation of the LTE vortex in this flow. The formation of the UTE vortex at $L/D = 10$ is shown in figure 17(*c*, *d*). The flow at $L/D = 15$ exhibits similar behaviour, so it is not presented here. At $t = t_0$ (in figure 17*c*), the UTE shear layer rolls up, generating two UTE vortices simultaneously. This double-TE vortex formation has not been reported in previous studies on the flows around rectangular cylinders. The UTE shear layer forms via KH instability, similar to the flow at $L/D = 10$ with $G/D = 0.1$, and does not deflect downstream, resulting in no upper recirculation behind the cylinder (in figures 8*c* and 8*e*). By $t = t_0 + 8\Delta t$ (in figure 17*d*), the upstream UTE vortex interacts with the ULE vortex, and breaks up. While the downstream one successfully develops into hairpin vortices. Despite the lifting of the LTE shear layer, no LTE vortex forms. This contrasts with the FNCC at $G/D = 0.3$ (Li *et al.* 2022*a*) and even at lower $G/D = 0.25$ (He *et al.* 2017), where the lower wake vortex forms and sheds, producing alternating vortex shedding dynamics.

As shown in figure 8, multiple recirculations are observed downstream of the cylinder. The corresponding instantaneous vortex dynamics is investigated using the clustering method (Jiménez *et al.* 2004; Dong *et al.* 2020; Wang *et al.* 2022*a*,*b*), previously effective in identifying secondary and tertiary vortices in the FNCC (Li *et al.* 2022*a*). Here, the criteria for identifying significant vortex structures through clustering methods are defined by $Q > 0.05$, with distinct characteristic structures differentiated by the positive or negative value of the spanwise vorticity ω_z. The extracted structures are shown in figure 18. Since the flow at $L/D = 15$ is similar to that at $L/D = 10$ (in figure 8), only the instantaneous structures for $L/D = 10$ are discussed. As illustrated in figure 18, the vortex structure distributions for $L/D = 5$ and $L/D = 10$ display notable similarities.

https://doi.org/10.1017/jfm.2025.365 Published online by Cambridge University Press

Secondary vortices with negative ω_z emerge downstream of the LTE shear layer. These vortices, positioned near the TE, are referred to as TSV. Immediately downstream, on the wall, vortex structures characterized by positive ω_z are observed, and are designated as WPV. This vortex distribution pattern closely resembles that observed in the FNCC at the same G/D (Li *et al.* 2022*a*), although the in the current flows, especially the secondary vortices, are less pronounced compared with those in the FNCC.

As shown in the inset of figure 18, in both two cases, the TSV originates from the plate boundary layer, driven by an adverse pressure gradient, as depicted by the smaller clockwise motion arrow near the plate wall. When the gap flow interacts with the downstream wall recirculation (the larger clockwise motion arrow), the WPVs forms. However, the dominant sources for WPV formation differ significantly with varying L/D values. For $L/D = 5$ (in the inset of figure 18*a*), the wall recirculation is more pronounced, competing effectively with the gap flow, which causes a significant upward deflection of the gap flow. Near the wall, the WPV (the anticlockwise motion arrow) forms as the wall recirculation encounters the TSV. The intense wall recirculation brings two clockwise recirculations into close proximity – the wall recirculation itself and the one induced by the TSV. This proximity causes the wall recirculation to absorb the TSV-induced recirculation within the mean field, as illustrated in figure 8(*a*). Consequently, aside from the wall recirculation, only anticlockwise recirculation corresponding to the WPV is observed in the mean field. When $L/D = 10$ (in the inset of figure 18*b*), the wall recirculation diminishes, and the gap flow extends farther downstream following the formation of the TSV. Upon encountering the wall recirculation, the gap flow lifts upwards, creating a local adverse flow that leads to WPV formation. Thus, the WPV primarily originates from the gap flow, differing from the scenario at $L/D = 5$. Meanwhile, the wall recirculation and TSV are effectively blocked by the WPV, resulting in their independent existence in the mean field, as shown in figure 8(*b*). A comparison between the FNCC and FNRC reveals that: in the FNCC, vortices with positive ω_z are induced by secondary vortices; while in the FNRC, they result from the competition between the gap flow and wall recirculation. The dominant source is influenced by L/D, which explains why these vortices (WPVs) are not named as TV in this study.

3.2.3. *The $G/D = 0.9$ cases*

For $L/D = 5$ and $G/D = 0.9$, the formation of the TE vortex is examined in figure 19. At $t = t_0$ (in figure 19*a*), the LTE sheds from the LTE shear layer, while the UTE shear layer rolls up. By $t = t_0 + 9\Delta t$ (in figure 19*b*), the LTE vortex has shed off and evolved into wake. The UTE shear layer deflects downward, strengthening the UTE vortex. Then, the alternating shedding of upper and lower trailing vortices occurs, differing from the dynamics at $G/D = 0.1$ and 0.3. Moreover, figure 19(*b*) shows the LLE vortex and TSV, with their formation depicted in figure 20.

As shown in figure 20(*a*), at time $t = t_0$, the LLE shear layer rolls up, forming the leading secondary vortex (LSV_3) from the plate wall. Notably, the LSV forms before the LLE vortex. The LSV_3 undergoes instability, causing plate boundary layer separation and forming the weak TV_2. The LLE vortex advances to $x/D \approx 4$, where LSV_2 forms, while LSV_1 is located near the TE, with LSV_2 being smaller than LSV_1. At $t = t_0 + 5\Delta t$ (in figure 20*b*), the LE shear layer rolls farther, creating a SV with negative ω_z, which quickly dissipates downstream. Meanwhile, the enhanced TV_2 stabilizes LSV_3, and the spanwise instability of the LLE vortex suppresses the growth of LSV_2. By $t = t_0 + 10\Delta t$ (in figure 20*c*), a new LLE vortex sheds. While the established one is transitioning into the LTE vortex. This transition does not occur in the FIRC (Cimarelli *et al.* 2018*b*, 2019*a*;

https://doi.org/10.1017/jfm.2025.365 Published online by Cambridge University Press

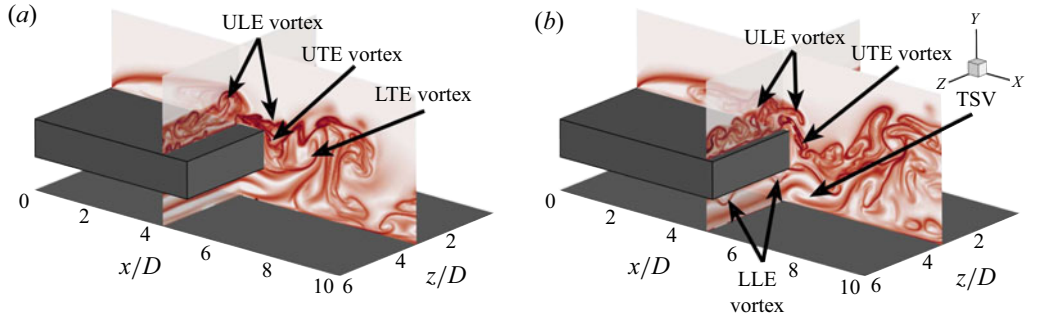


Figure 19. The evolution process of the UTE vortex revealed by LCSs presented in the slices for $L/D = 5$ and $G/D = 0.9$: (*a*) $t = t_0$; (*b*) $t = t_0 + 9\Delta t$, where $\Delta t = 0.25D/U_0$.

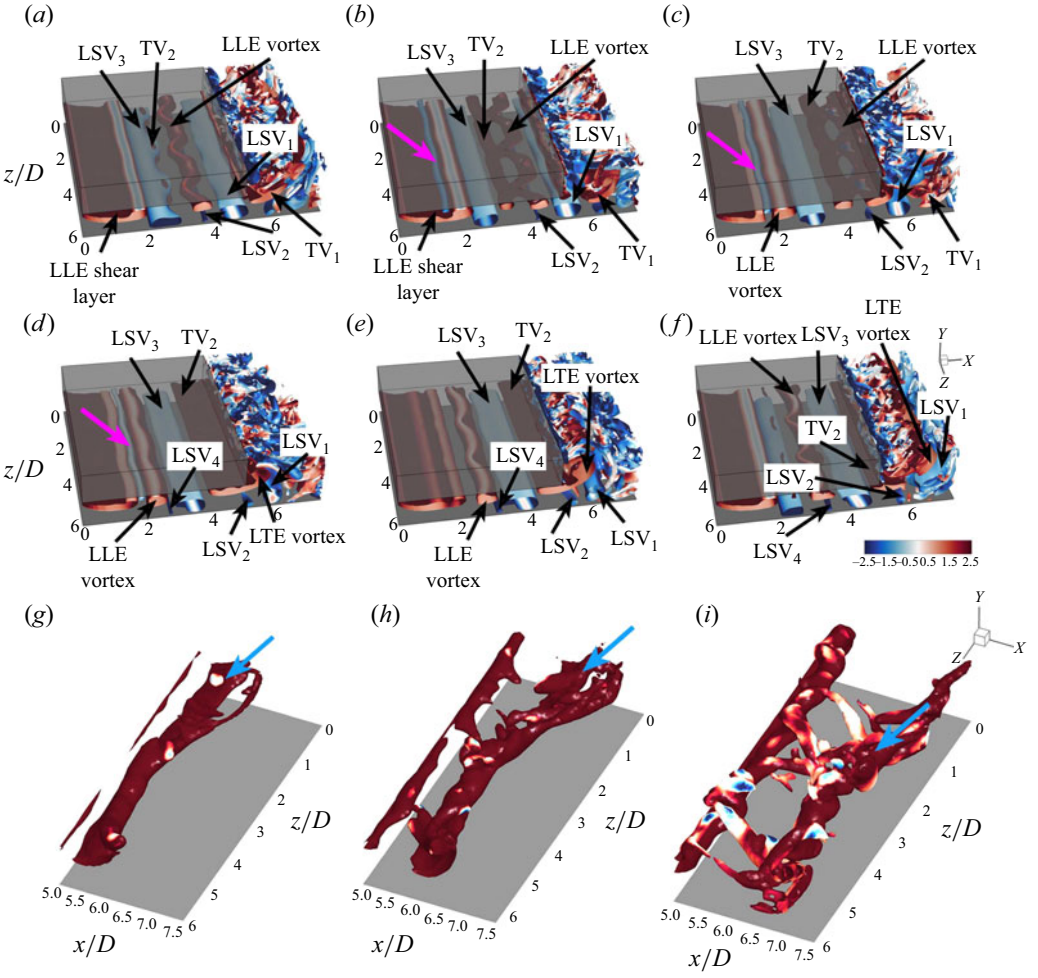


Figure 20. The vortex dynamics in the gap at $L/D = 5$ and $G/D = 0.9$: (*a*) $t = t_0$; (*b*) $t = t_0 + 5\Delta t$; (*c*) $t = t_0 + 10\Delta t$; (*d*) $t = t_0 + 15\Delta t$; (*e*) $t = t_0 + 20\Delta t$; (*f*) $t = t_0 + 25\Delta t$, where $\Delta t = 0.25D/U_0$. Here (*g*), (*h*) and (*i*) are partial structures extracted from (*a*), (*b*) and (*c*), respectively. The vortical structures are visualized by isosurfaces of $Q = 0.1$, coloured with the instantaneous spanwise vorticity ω_z. The magenta arrow marks the SV with negative ω_z on the lower side of the cylinder. The azure arrow marks TV_1.

https://doi.org/10.1017/jfm.2025.365 Published online by Cambridge University Press

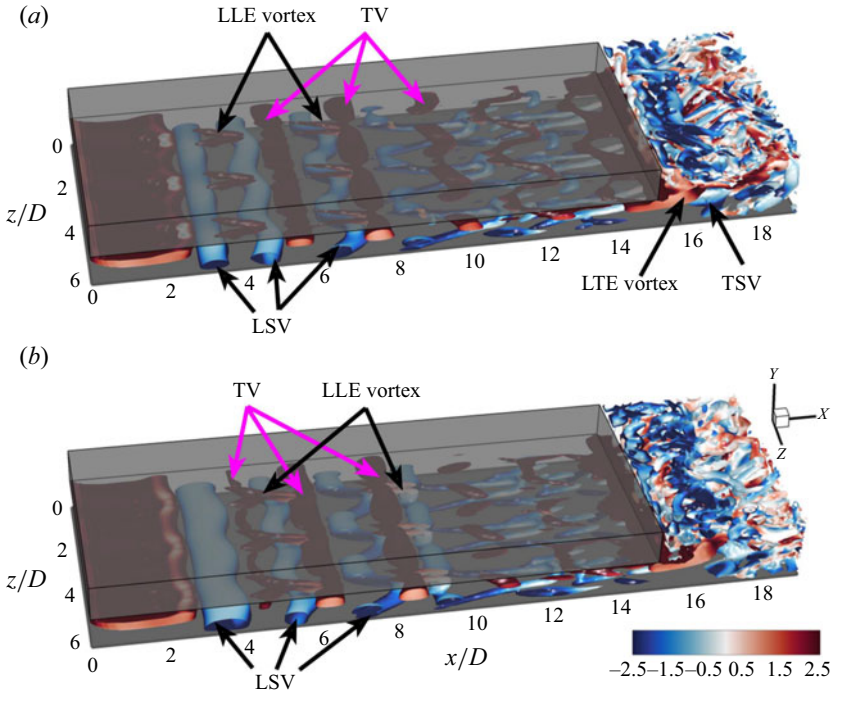


Figure 21. The vortex dynamics in the gap at $L/D = 15$ and $G/D = 0.9$: (*a*) $t = t_0$; (*b*) $t = t_0 + 7\Delta t$; where $\Delta t = 0.25D/U_0$. The vortical structures are visualized by isosurfaces of $Q = 0.1$, coloured with the instantaneous spanwise vorticity ω_z.

Chiarini & Quadrio 2021; Chiarini *et al.* 2021, 2022*a*; Zhang *et al.* 2023; Cimarelli *et al.* 2024; Li *et al.* 2024*b*). The LSV_1 convects downstream while LSV_2 fragments. At $t = t_0 + 15\Delta t$ (in figure 20*d*), a weaker SV (LSV_4) forms, indicating that each LLE vortex can induce two secondary vortices in one shedding cycle. The LTE vortex interacts with LSV_1, and TV_2 flattens and merges into the LTE vortex. At $t = t_0 + 20\Delta t$ (in figure 20*e*), the LTE vortex lifts, causing LSV_1 to rise. The LSV_2, previously fragmented, is enhanced by the LTE vortex. At $t = t_0 + 25\Delta t$ (in figure 20*f*), the LTE vortex sheds off, and LSV_1 deforms and rises. The LSV_2 is enhanced but no new SV forms near the LTE. The separation of the wall boundary layer near the LTE results from the established weak LSV. The TV_2 does not shed with the LTE vortex; instead, it forms a pseudo-TE vortex, with its shedding corresponding to the evolution of TV_1 (in figure 20$a-c$), which is extracted through the clustering method and shown in figure 20($g-i$). After shedding, TV_2 does not rise like the LTE vortex but convects downstream. Double-secondary vortices, similar to those observed in multielement airfoils (Wang, Wang & Kim 2019; Wang & Wang 2021*b*) and simplified circular-cylinder/airfoil configurations (Wang, Wu & Wang 2023), also appear in the FNCC boundary layer at $G/D = 1.0$ and 1.333 (Wang *et al.* 2024). However, the secondary vortices in this study are smaller and weaker, distinguishing them from previous double-SV configurations.

The vortex dynamics at $L/D = 10$ will be discussed in § 3.3.1, influenced by two distinct frequencies. For $L/D = 15$, as shown in figure 21, vortex formation is similar to $L/D = 5$, but no double-secondary vortices form from the plate boundary layer. The LKH vortex rapidly evolves into the LLE vortex in the form of a streamwise vortex pair, as shown in figure 21(*a*). Figure 21(*b*) indicates the LSV exhibits spanwise instability, reversely inducing lower boundary layer separation and forming a TV, as at $L/D = 5$. Unlike at

https://doi.org/10.1017/jfm.2025.365 Published online by Cambridge University Press

$L/D = 5$, the LSV does not return to a two-dimensional structure, instead stretching into hairpin-like vortices. The TV strengthens under the influence of TSV but breaks up due to mean shear. Two adjacent TV groups merge near the LTE, forming an LTE vortex, which induces a TSV from the plate boundary layer.

3.3. *Frequency characteristics*

In the FIRC at medium Re, the LE and TE vortices shed at the same frequency for a fixed L/D, exhibiting frequency locking. Multiple KH vortices merge to form a cohesive LE vortex. These dynamics can be reflected in the PSD (Wang & Wang 2021*a*; Tian *et al.* 2023; Duan & Wang 2024; Li *et al.* 2024*b*; Zhang *et al.* 2024; Zhou *et al.* 2024). The influence of near-wall effects on frequency characteristics and vortex dynamics will be examined in the context of the FIRC.

3.3.1. *Flow processes with typical frequencies*

The PSDs are calculated at the azure points in figure 13, and remain marked by the same numbers. The velocity fluctuations at this location are typically the highest locally, particularly at points 1–3, which are distributed along the shear layer. The characteristic peaks detected at nearly all monitoring points within a flow can be used to identify the corresponding characteristic frequency of the flow. Figure 22(a, c, e), show the PSDs at various spatial positions for different L/D ratios at $G/D = 0.1$. For $L/D = 5$, as illustrated in figure 22(a), a prominent fluctuation signal is observed from the LE shear layer extending to the downstream wall recirculation, which corresponds to the fundamental frequency St_0 and is characteristic of the LE vortex dynamics. Probes 1–3 show $0.5St_0$ (marked by the red circle), $1.5St_0$ (marked by the blue circle) and St_{KH} ($St_{KH} = 2St_0$), with the subharmonic $0.5St_0$ and fractional harmonic $1.5St_0$ resulting from nonlinear interactions. The St_{KH} weakens downstream and represents the fluctuation frequency of KH instability within the ULE shear layer. The relation $St_{KH} = 2St_0$ indicates that every two UKH vortices merge to form a single ULE vortex during one shedding cycle. In contrast, in the FIRC at $L/D = 5$, every three KH vortices merge into one LE vortex (Zhang *et al.* 2023; Li *et al.* 2024*b*). The merging process of UKH vortices for $G/D = 0.1$ and $L/D = 5$ is shown in figure 23. Instantaneous vortices visualized with isosurfaces of $Q = 0.5$ reveal that adjacent UKH vortices shed from the ULE shear layer, merging downstream, as shown in figure 23($a - d$). After merging, the vortex becomes 3-D and evolves into the ULE vortex. Notably, the UKH vortices merge before undergoing 3-D instability here, whereas in the FIRC, instability occurs first (Zhang *et al.* 2023). The near-wall effect influences both the number and sequence of merging and instability. Furthermore, figure 22(a) shows consistent characteristic frequencies across all probes, including in the downstream recirculation, indicating that the frequency-locking feature persists in the FNRC with $L/D = 5$ and $G/D = 0.1$.

For $L/D = 10$ and $G/D = 0.1$, figure 22(c) shows the fundamental frequency St_0 in the PSDs for all probes. Additionally, a new frequency St_{0*}, similar to St_0, is detected in probes 1 and 2 within the ULE shear layer but weakens and disappears downstream. This is interpreted as a pseudoshedding frequency, to be validated by DMD analysis in § 3.3.2. In probe 1, the dominant frequency with a wide bandwidth is St_0, indicating that the ULE vortex primarily originates from a single UKH vortex. The evolution of the ULE vortex from the UKH vortex is shown in figure 24. Notably, adjacent UKH vortices do not merge but directly evolve into ULE vortices in the form of hairpin vortices. In contrast, in the FIRC with $L/D = 10$, every two KH vortices merge to form an LE vortex (Li *et al.* 2024*b*). As L/D increases to 15, figure 22(d) shows two distinct shedding frequencies, St_{01} and

https://doi.org/10.1017/jfm.2025.365 Published online by Cambridge University Press

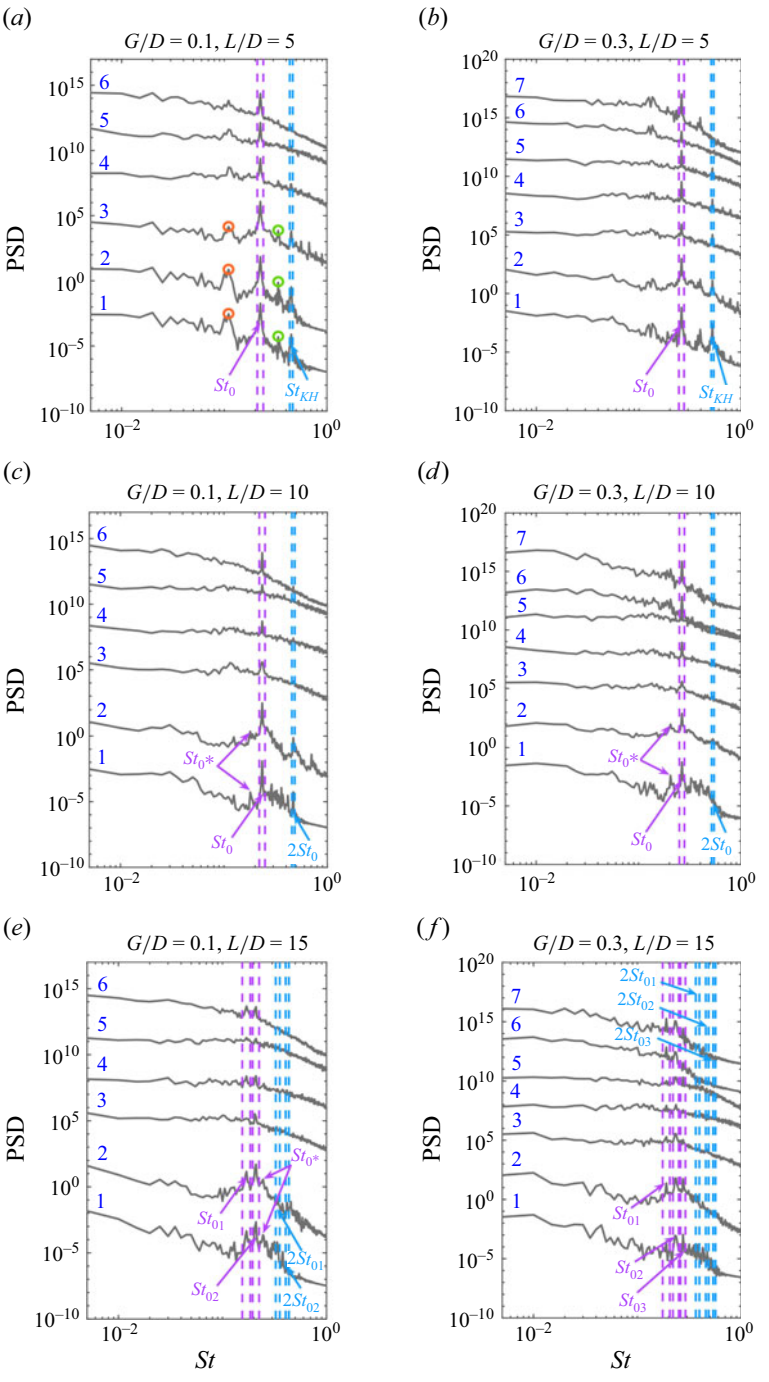


Figure 22. Local PSDs of streamwise velocity fluctuation at different spatial locations for $G/D = 0.1$ and $G/D = 0.3$: (*a,c,e*) $G/D = 0.1$; (*b,d,f*) $G/D = 0.3$; (*a,b*) $L/D = 5$; (*c,d*) $L/D = 10$; (*e,f*) $L/D = 15$. The PSDs are calculated at azure points in figure 13(*a,b*) and remain marked by the same numbers. The amplitudes of PSDs for azure point 2−7 are amplified step-by-step by 10^3 along the serial number. Here St_0, St_{01}, St_{02} and St_{03} denote the shedding frequencies of the LE or TE vortex; St_{0*} is the pseudoshedding frequency; St_{KH} is KH fluctuation frequency. The orange circle marks $0.5St_0$, while the lime green circle marks $1.5St_0$. The dashed lines define the frequency bands with a bandwidth of 0.02, related to the typical frequencies.

https://doi.org/10.1017/jfm.2025.365 Published online by Cambridge University Press

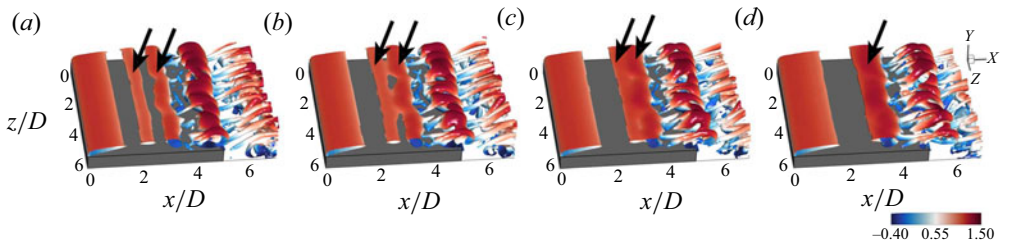


Figure 23. The process of the UKH vortex merging at $G/D = 0.1$ and $L/D = 5$: (*a*) $t = t_0$; (*b*) $t = t_0 + 2\Delta t$; (*c*) $t = t_0 + 4\Delta t$; (*d*) $t = t_0 + 6\Delta t$, where $\Delta t = 0.25D/U_0$. The vortical structures are visualized by isosurfaces of $Q = 0.5$, coloured with the instantaneous streamwise velocity u/U_0. The black arrow marks the UKH vortex.

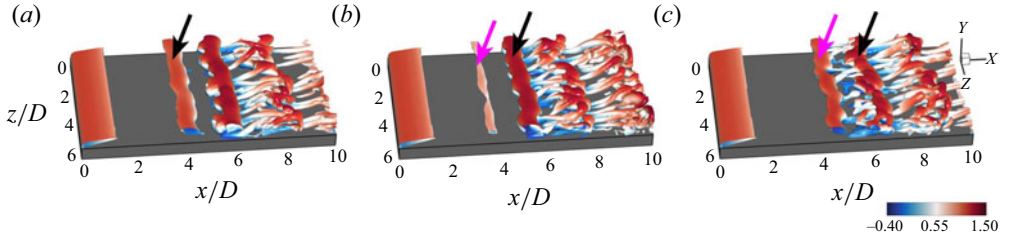


Figure 24. The process of the UKH vortex evolving into the ULE vortex at $G/D = 0.1$ and $L/D = 10$: (*a*) $t = t_0$; (*b*) $t = t_0 + 10\Delta t$; (*c*) $t = t_0 + 20\Delta t$, where $\Delta t = 0.25D/U_0$. The vortical structures are visualized by isosurfaces of $Q = 0.5$, coloured with the instantaneous streamwise velocity u/U_0. The arrow marks the UKH vortex.

St_{02}, due to mode competition, which will be discussed further in the DMD analysis in § 3.3.2. The evolution of the UKH vortex into the ULE vortex at $L/D = 15$ is similar to $L/D = 10$. For $G/D = 0.3$, the PSDs for different L/D ratios (in figure 22*b*, *d*, *f*) are similar to those at $G/D = 0.1$, except at $L/D = 15$, where three-mode competition arises.

The local PSDs for $G/D = 0.9$ are presented in figure 25. For $L/D = 5$, figures 25(*a*) and 25(*b*) show the fundamental frequency St_0 is present in all probes, confirming frequency locking and that the characteristic frequency of SV coincides with St_0. A high-frequency band at four times St_0 suggests four UKH vortices shed from the ULE shear layer in one LE/TE shedding cycle. The evolution of this process is illustrated in figure 26. At $t = t_0$ (figure 26*a*), UKH_1 and UKH_2 form, while the LTE shear layer rolls up to create an LTE vortex. The UKH_1 evolves into hairpin vortices, while UKH_2 strengthens the LTE vortex (in figure 26*b* and 26*c*). By $t = t_0 + 15\Delta t$ (in figure 26*d*), UKH_3 forms and, along with UKH_2, merges to form the ULE vortex (in figure 26*e*), with the LTE vortex shedding off. As shown in figure 26(*f*), the merged vortex separates, while a new UKH vortex (UKH_4) begins to form. Notably, although four UKH vortices are generated, not all participate in merging. The PSDs from probes 7 and 8 show harmonics of St_0, attributed to downstream convection of the TV and the enhancement of the weak LSV, resembling the harmonics seen in double-secondary vortices in the FNCC (Wang *et al.* 2024).

The PSDs for $L/D = 10$ and $G/D = 0.9$ are illustrated in figures 25(*c*) and 25(*d*). Two dominant frequencies, St_{01} and St_{02}, are observed. At probe 1, both frequencies are distinct, but at probes 2 and 3, St_{02} becomes dominant, while St_{01} weakens. The wide bandwidth at probes 1 and 2 indicates that a single ULE vortex evolves from a UKH vortex, with shedding frequency St_{02}. At probe 4, downstream, St_{01} reappears, signalling double-mode competition as the flow becomes more complex and wall boundary layer

https://doi.org/10.1017/jfm.2025.365 Published online by Cambridge University Press

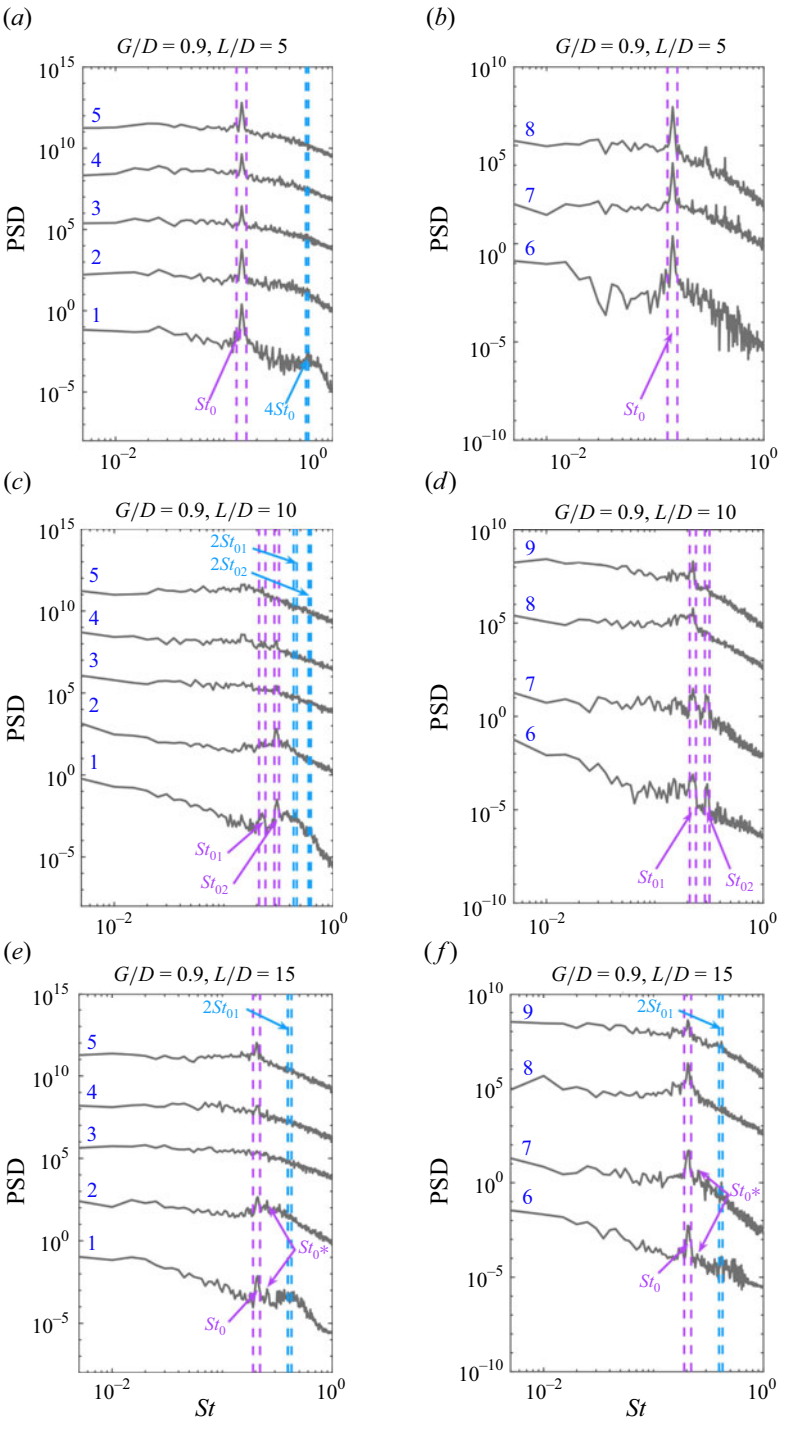


Figure 25. Local PSDs of streamwise velocity fluctuation at different spatial locations for $G/D = 0.9$: (*a*,*b*) $L/D = 5$; (*c*,*d*) $L/D = 10$; (*e*,*f*) $L/D = 15$. The PSDs are calculated at azure points in figure 13(*c*) and remain marked by the same numbers. The amplitudes of PSDs for azure point 2−5 and 7−9 are amplified step-by-step by 10^3 along the serial number. Here St_0, St_{01} and St_{02} denote the shedding frequencies of the LE or TE vortex; St_{0*} is the pseudoshedding frequency. The dashed lines define the frequency bands with a bandwidth of 0.02, related to the typical frequencies.

https://doi.org/10.1017/jfm.2025.365 Published online by Cambridge University Press

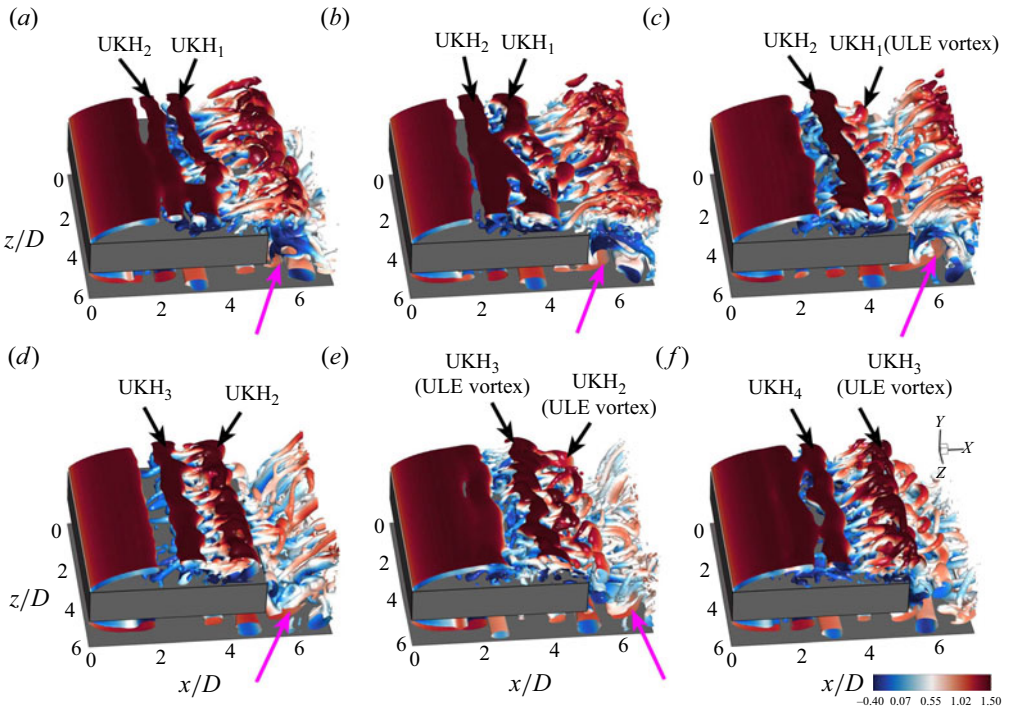


Figure 26. The process of the UKH vortex evolving into the ULE vortex at $G/D = 0.9$ and $L/D = 5$: (*a*) $t = t_0$; (*b*) $t = t_0 + 5\Delta t$; (*c*) $t = t_0 + 10\Delta t$; (*d*) $t = t_0 + 15\Delta t$; (*e*) $t = t_0 + 20\Delta t$; (*f*) $t = t_0 + 25\Delta t$, where $\Delta t = 0.25D/U_0$. The vortical structures are visualized by isosurfaces of $Q = 0.5$, coloured with the instantaneous streamwise velocity u/U_0. The magenta arrow marks the LTE vortex.

characteristics emerge (in figure 6*b*). At probe 5, near the UTE vortex shedding location, a reduction in the peaks of both frequencies occurs, with St_{01} still detectable and St_{02} disappearing, indicating the UTE vortex shedding frequency is St_{01}. This marks a shift in the characteristic frequency from St_{02} to St_{01} on the upper side of the cylinder. At probe 6, within the LLE shear layer, both St_{01} and St_{02} remain, but no wide bandwidth is observed, suggesting bimodal competition in LLE vortex formation. At probes 8 and 9, associated with the LTE vortex shedding and TSV formation, the frequency is St_{01}, with St_{02} diminishing. This shows that frequency locking is suppressed in the flow at $G/D = 0.9$ and $L/D = 10$.

The presence of two dominant frequencies warrants investigation into their effects on vortex dynamics. The signals for St_{01} and St_{02} are extracted via Fourier mode decomposition (Basley *et al.* 2011; Ma *et al.* 2015; Wang *et al.* 2018; Wang & Wang 2021*a*,*b*; Li *et al.* 2024*b*) from probe 7 at $z/D = \pi$, as shown in figure 13(*ci*). The results, presented in figure 27, show strong competition between the two frequencies: when St_{01} fluctuates strongly, St_{02} weakens and *vice versa*. Specifically, around time $t = t_a$, the fluctuation is dominated by St_{01}, while St_{02} is weak; the reverse occurs at $t = t_b$. The vortex dynamics for $L/D = 10$ and $G/D = 0.9$ in figure 28 resemble those at $L/D = 15$ and $G/D = 0.9$ (in figure 21), but the SV evolution differs between the two frequencies. When St_{01} is dominant, hairpin-like vortices form from the LSV (in figures 28*a* and 28*b*), as seen at $L/D = 15$. In contrast, when St_{02} dominates, no hairpin vortices form, and only spanwise vortices are present (in figures 28*c* and 28*d*). Additionally, with St_{01}, the LTE vortex sheds before the TV reaches the LTE, whereas for St_{02}, the LTE vortex has not

https://doi.org/10.1017/jfm.2025.365 Published online by Cambridge University Press

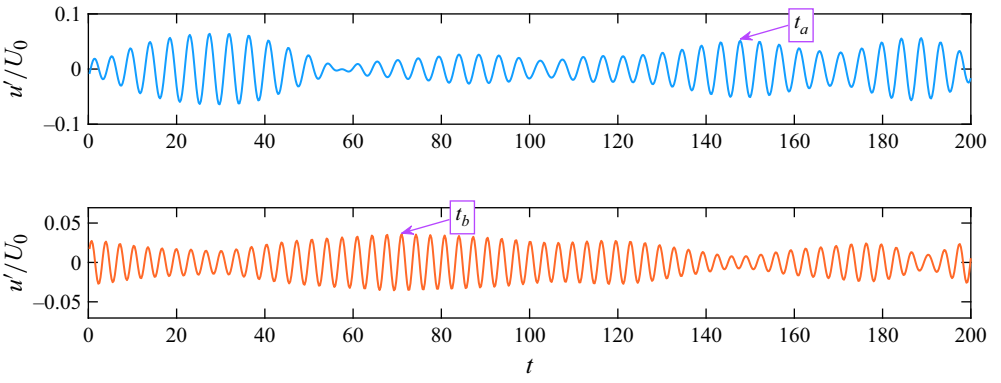


Figure 27. The time signals of streamwise velocity fluctuation for St_{01} and St_{02} at $L/D = 10$ and $G/D = 0.9$. The azure and orange curves are the signals of the Fourier mode decomposition mode for St_{01} and St_{02}, respectively, which are extracted from the probe 7 (presented in figure 13*c* i) in the plane $z/D = \pi$. Here t_a and t_b mark the typical instances for the strong fluctuations of St_{01} and St_{02}, respectively.

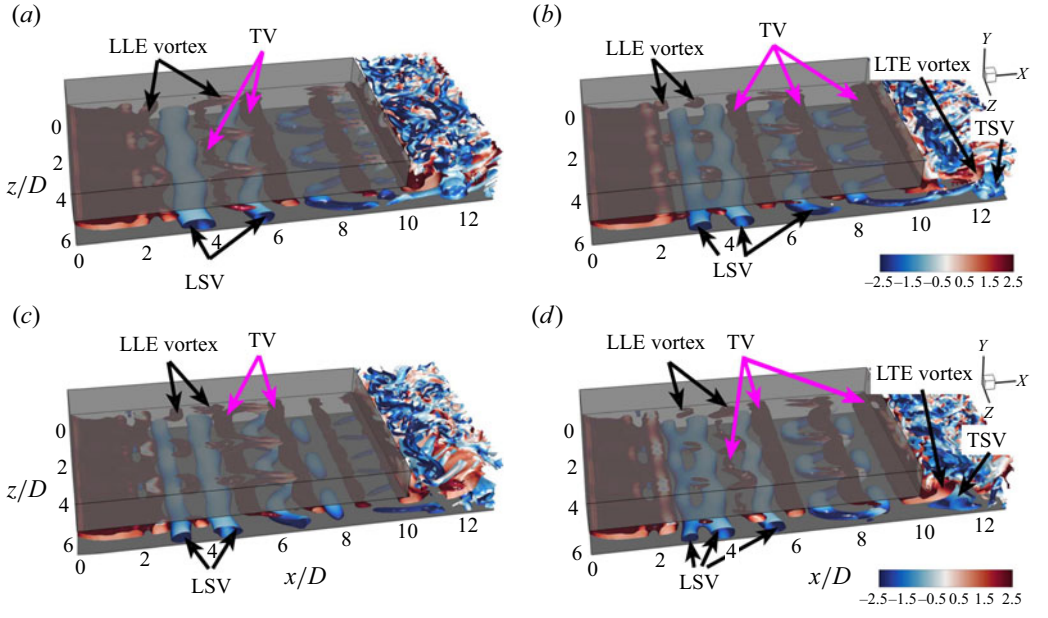


Figure 28. The instantaneous vortical structures in the gap for $L/D = 10$ and $G/D = 0.9$: (*a*) $t = t_a - 8\Delta t$; (*b*) $t = t_a$; (*c*) $t = t_b - 8\Delta t$; (*d*) $t = t_b$, where $\Delta t = 0.25D/U_0$. The vortical structures are visualized by isosurfaces of $Q = 0.1$, coloured with the instantaneous spanwise vorticity ω_z.

yet shed at that point. This phase difference results from the competition between the two frequencies but does not affect the characteristic frequencies of the LTE vortex and TSV, as shown in figure 25(*d*) at probes 8 and 9.

As L/D increases to 15, the PSDs in figures 25(*e*) and 25(*f*) show a single fundamental frequency, St_0, across all probes, indicating frequency locking despite the presence of a pseudofrequency related to vortex shedding. In the PSD at probe 1 within the ULE shear layer, the dominant high-frequency bandwidth is $2St_0$, suggesting that two UKH vortices merge to form one ULE vortex. This is illustrated in figure 29, where two adjacent UKH vortices shed from the ULE shear layer (in figure 29*a*), interact with the ULE recirculation

https://doi.org/10.1017/jfm.2025.365 Published online by Cambridge University Press

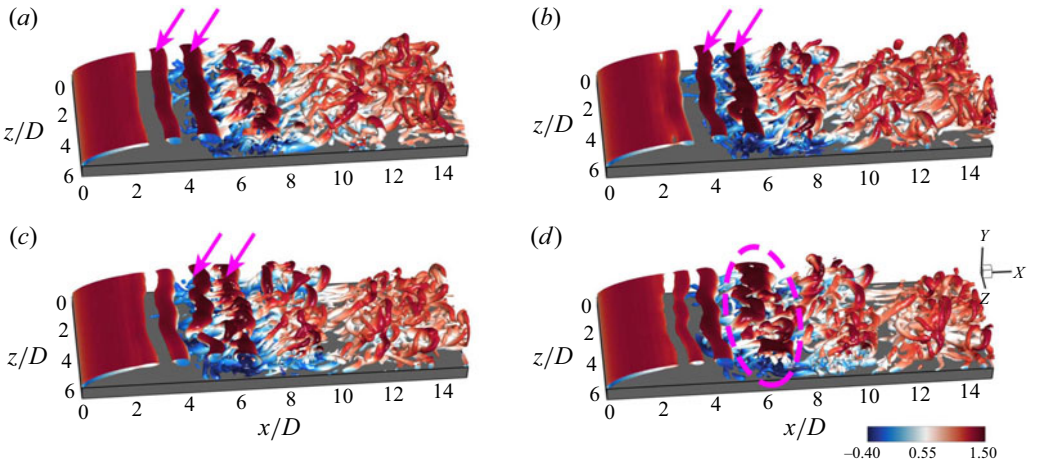


Figure 29. The process of the UKH vortex evolving into the ULE vortex at $L/D = 15$ and $G/D = 0.9$: (*a*) $t = t_0$; (*b*) $t = t_0 + 5\Delta t$; (*c*) $t = t_0 + 10\Delta t$; (*d*) $t = t_0 + 15\Delta t$, where $\Delta t = 0.25D/U_0$. The vortical structures are visualized by isosurfaces of $Q = 0.5$, coloured with the instantaneous streamwise velocity u/U_0. The magenta arrow marks the UKH vortex, and the ellipse marks the ULE vortex in the form of the hairpin vortex cluster.

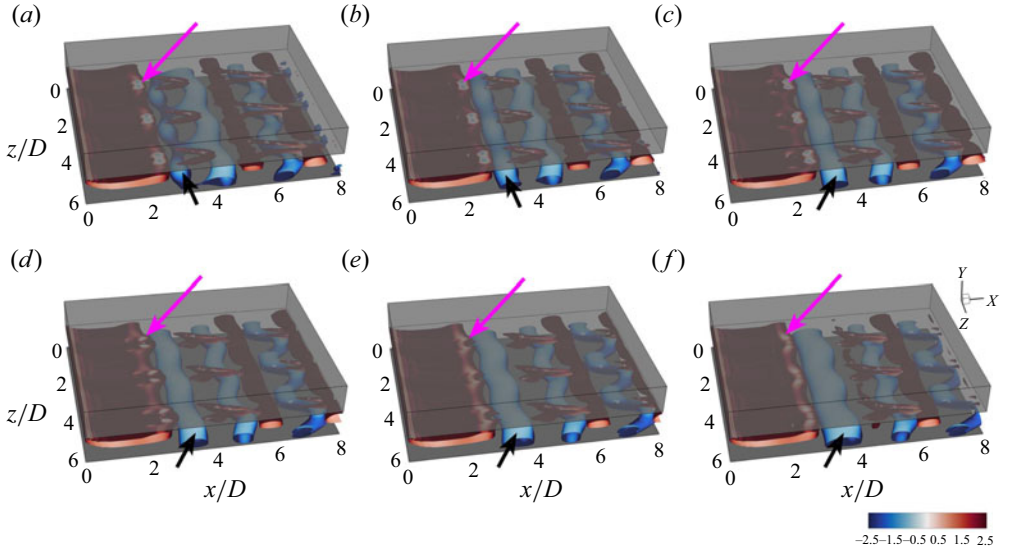


Figure 30. The process of LLE vortex shedding being suppressed at $L/D = 15$ and $G/D = 0.9$: (*a*) $t = t_0$; (*b*) $t = t_0 + 2\Delta t$; (*c*) $t = t_0 + 4\Delta t$; (*d*) $t = t_0 + 6\Delta t$; (*e*) $t = t_0 + 8\Delta t$; (*f*) $t = t_0 + 10\Delta t$, where $\Delta t = 0.25D/U_0$. The vortical structures are visualized by isosurfaces of $Q = 0.1$, coloured with the instantaneous spanwise vorticity ω_z. The black arrow marks the LSV, the magenta arrow marks the LLE shear layer.

(in figure 29*b*), and evolve into 3-D vortices (in figure 29*c*). They then merge to form a ULE vortex, a hairpin vortex cluster (in figure 29*d*). This process, where UKH vortices first undergo 3-D instability before merging, contrasts with the behaviour at $L/D = 5$ and $G/D = 0.1$ (in figure 23). Additionally, figure 25(*f*) shows a wide bandwidth around $2St_0$ at probe 6, but the merging of LKH vortices into an LLE vortex does not occur here. This suppression occurs because the enhanced LSV inhibits the formation of KH vortices when the LLE shear layer undergoes the second KH instability. As a result,

https://doi.org/10.1017/jfm.2025.365 Published online by Cambridge University Press

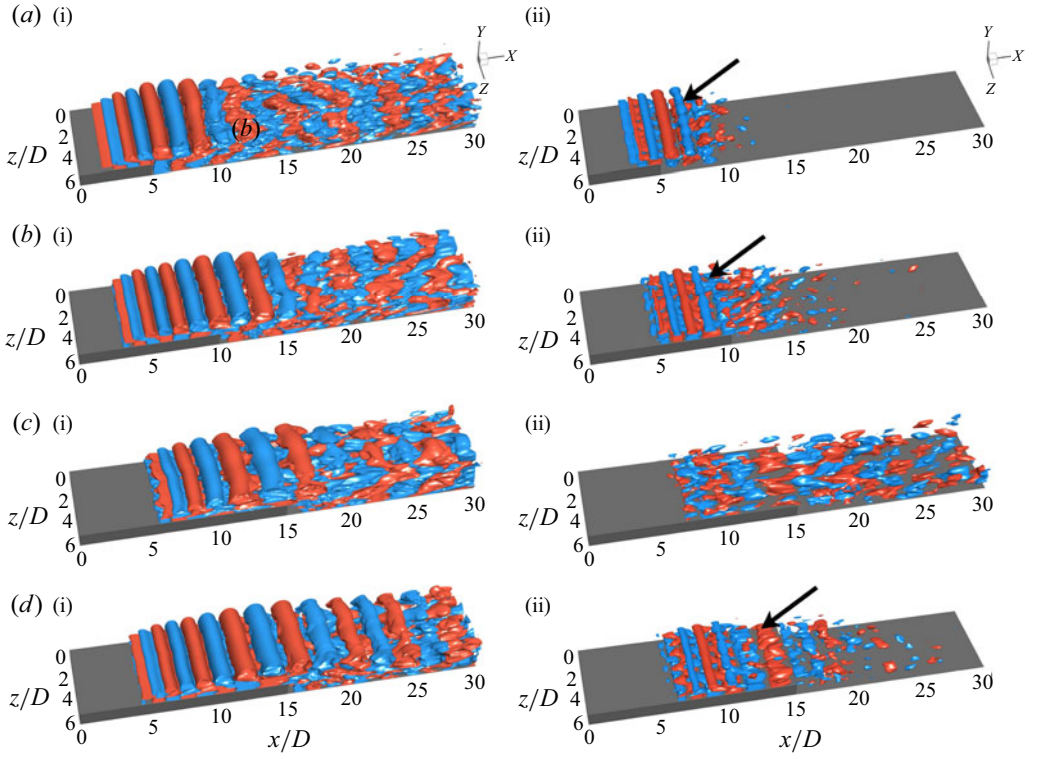


Figure 31. Isosurfaces of the real part of the DMD mode for the streamwise component at $G/D = 0.1$: (*a*) St_0 mode for $L/D = 5$; (*b*) St_0 mode for $L/D = 10$; (*c*) St_{01} mode for $L/D = 15$; (*d*) St_{02} mode for $L/D = 15$. (i) The values are ± 0.0001; (ii) the values are ± 0.0005. The red parts are positive and the blue parts are negative. The arrows mark the periodic topological structures.

only the first KH instability contributes to the formation of KH vortices within a single shedding cycle. As shown in figure 30, the LKH vortex quickly evolves into the LLE vortex and experiences local instability figure 30(*b*–*d*). However, as the LSV strengthens, it suppresses the instability of the LLE shear layer figure 30(*e*–*f*), preventing the formation of additional LKH vortices during the same shedding cycle.

3.3.2. *Dynamic mode decomposition analysis*

To further investigate the dynamic characteristics of vortex shedding in the current FNRC, the DMD method is employed, akin to the analyses conducted on the FNCC (Li *et al.* 2022*a*) and FIRC (Zhang *et al.* 2023; Li *et al.* 2024*b*). This approach aims to explore the spatial characteristics of vortex shedding frequencies across all flows examined. Particular attention will be directed towards flows exhibiting multiple characteristic shedding frequencies, with the DMD method utilized to identify the dominant frequency for each flow.

Figure 31 illustrates the DMD analysis of ULE/UTE vortex shedding for flows with $G/D = 0.1$. The displayed topology represents the streamwise component of the DMD mode, with the structures in figures 31(*a*i) to 31(*d*i) showing similarities across different flows. These topological structures exhibit a regular alternating pattern in the streamwise direction, confirming the periodic nature of the flow and the presence of frequency

https://doi.org/10.1017/jfm.2025.365 Published online by Cambridge University Press

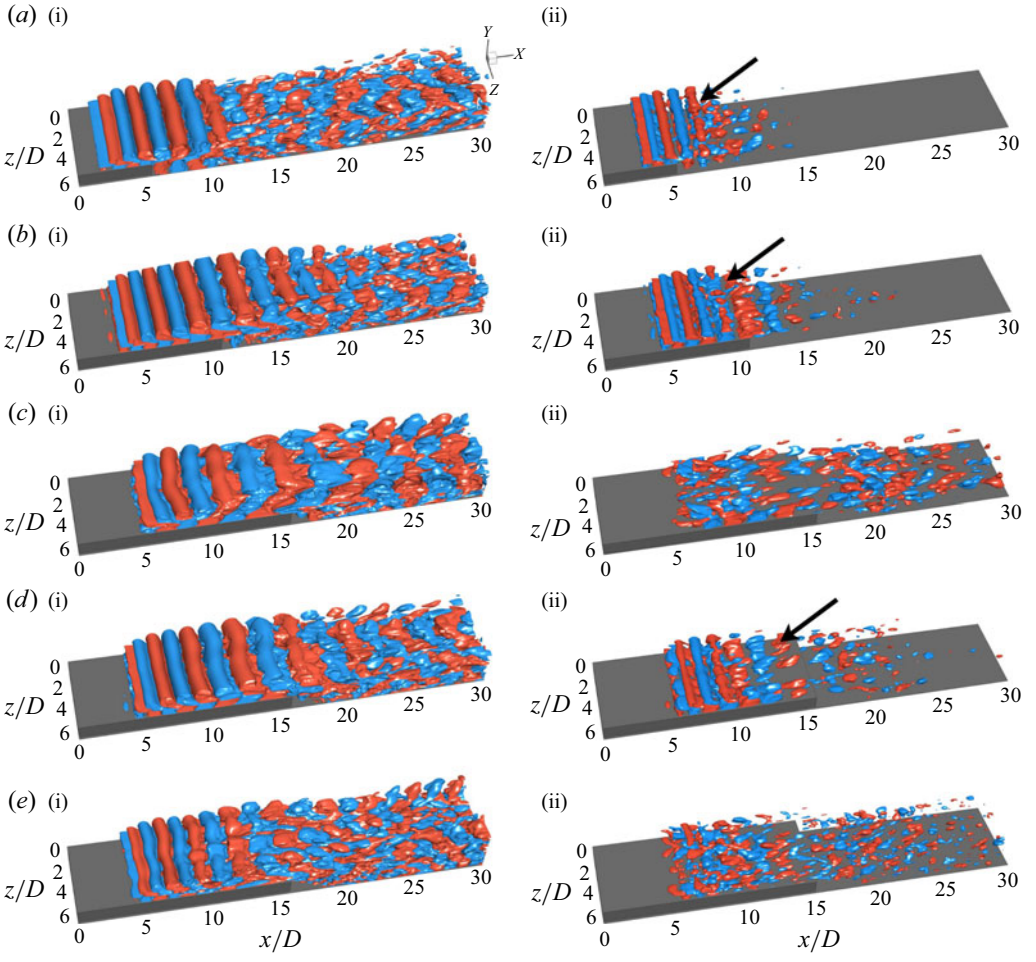


Figure 32. Isosurfaces of the real part of the DMD mode for the streamwise component at $G/D = 0.3$: (*a*) St_0 mode for $L/D = 5$; (*b*) St_0 mode for $L/D = 10$; (*c*) St_{01} mode for $L/D = 15$; (*d*) St_{02} mode for $L/D = 15$; (*e*) St_{03} mode for $L/D = 15$. (i) The values are ± 0.0001; (ii) the values are ± 0.0005. The red parts are positive and the blue parts are negative. The arrows mark the periodic topological structures.

locking. At $L/D = 15$, both St_{01} and St_{02} modes show periodicity, indicating competition between the two modes. However, the St_{02} mode is more pronounced and persists farther downstream (in figure 31*d*i). To identify the dominant shedding mode, the isosurface values of the DMD mode are increased, showing stronger fluctuations in figures 31(*a*ii) to 31(*d*ii). The DMD topological structures for St_0 at $L/D = 5$ and $L/D = 10$ and St_{02} at $L/D = 15$ maintain great coherence, reflecting flow periodicity. However, as the flow enters the plate boundary layer state, the stronger fluctuations dissipate, and the coherence of the St_{01} mode at $L/D = 15$ nearly disappears. Thus, the dominant frequency for the flow at $L/D = 15$ and $G/D = 0.1$ is St_{02}.

For $G/D = 0.3$, the DMD vortex shedding topologies are presented in figure 32. The topological structures in figures 32(*a* i) to 32(*e* i) exhibit strong periodicity, similar to those at $G/D = 0.1$, until the flow transitions into the boundary layer state. The St_{0*} mode at $L/D = 10$, representing the pseudoshedding frequency, is shown in figure 34(*a*) with

https://doi.org/10.1017/jfm.2025.365 Published online by Cambridge University Press

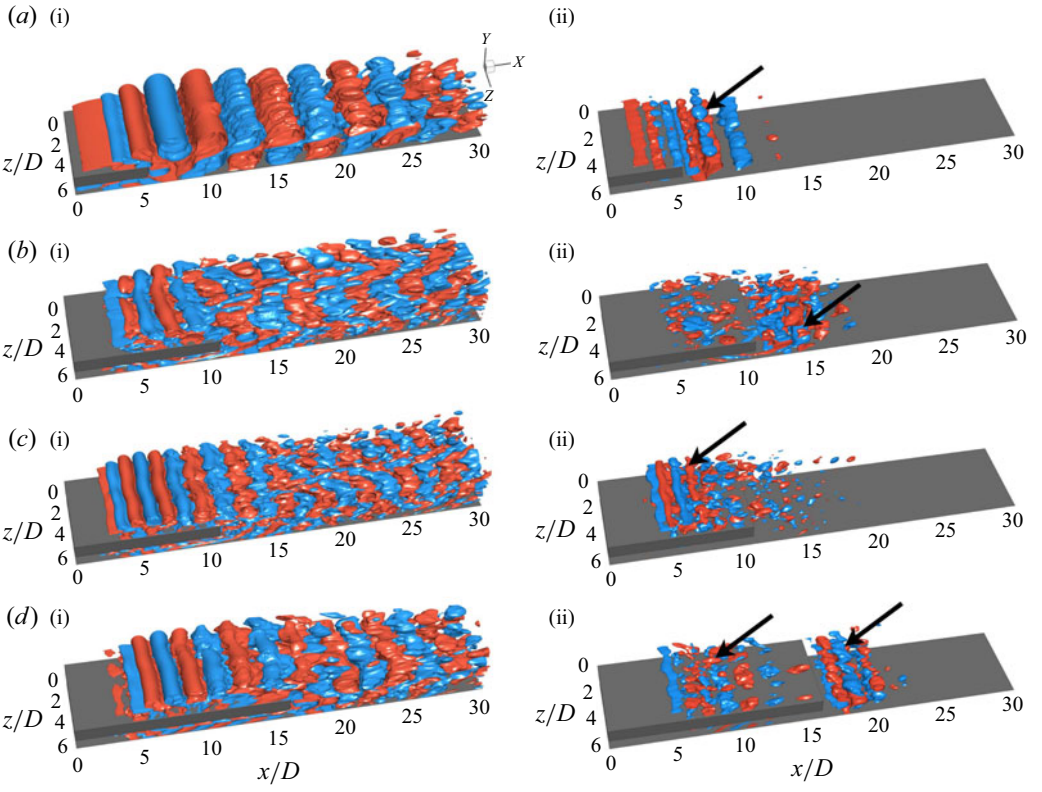


Figure 33. Isosurfaces of the real part of the DMD mode for the streamwise component at $G/D = 0.9$: (*a*) St_0 mode for $L/D = 5$; (*b*) St_{01} mode for $L/D = 10$; (*c*) St_{02} mode for $L/D = 10$; (*d*) St_0 mode for $L/D = 15$. (i) The values are ± 0.0001; (ii) the values are ± 0.0005. The red parts are positive and the blue parts are negative. The arrows mark the periodic topological structures.

identical isosurface values. This mode lacks spatial coherence, explaining its inability to capture flow periodicity and justifying its designation as a pseudoshedding frequency. The topologies for stronger fluctuations, shown in figures 32(*a*ii) to 32(*e*ii), reveal that the St_0 modes at $L/D = 5$ and $L/D = 10$ maintain great periodicity. However, at $L/D = 15$, only the St_{02} mode exhibits coherence, indicating it as the dominant mode despite the presence of three competing shedding frequencies. The St_{0*} mode at $L/D = 10$ continues to lack spatial coherence, as shown in figure 34(*b*).

As G/D increases to 0.9, all topological structures capture the periodicity of vortex shedding, similar to the smaller gap ratios, as shown in figures 33(*a*i) to 33(*d*i). These structures confirm the instability of the LLE shear layer, leading to vortex formation. At $L/D = 5$, the mode exhibits a Kármán vortex street pattern, indicating a reduced near-wall effect. At $L/D = 10$, the St_{02} mode shows greater coherence than St_{01}, with topologies capturing the periodicity of the LE and TE vortices. However, the St_{01} mode captures the periodicity of UTE and LTE vortices, while St_{02} reflects the ULE vortex but loses coherence near the TE. Thus, the St_{01} mode governs UTE and LTE vortices shedding, while St_{02} regulates ULE vortices shedding. This agrees with the PSDs in figures 25(*c*) and 25(*d*), confirming the suppression of frequency locking at $L/D = 10$ and $G/D = 0.9$. Figures 34(*c*) and 34(*d*) show the DMD topologies of the stronger fluctuations for St_{01} and St_{02} modes. Near the LTE, the St_{01} mode shows elongated streamwise features from the LSV, while St_{02} lacks these structures. These topologies correlate with the vortices in

https://doi.org/10.1017/jfm.2025.365 Published online by Cambridge University Press

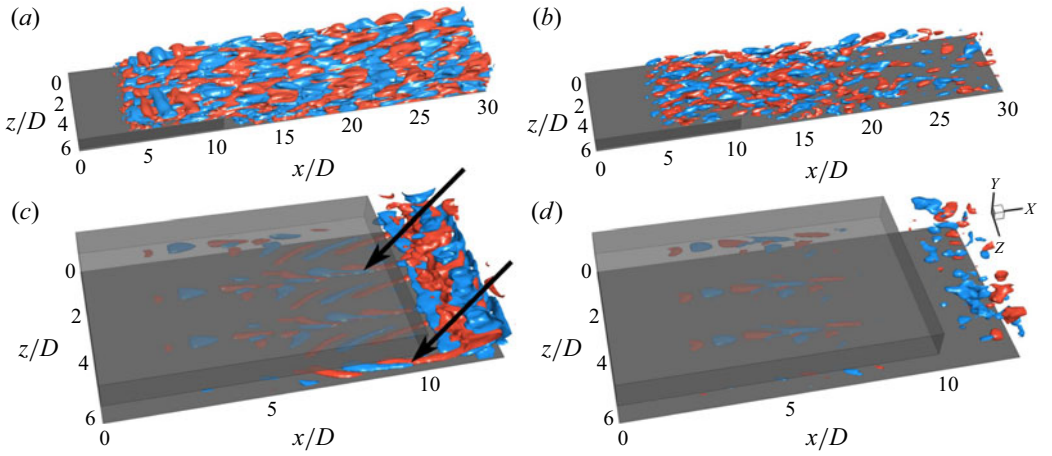


Figure 34. Isosurfaces of the real part of the DMD mode for the streamwise component: (*a,b*) St_{0*} mode for $L/D = 10$ and $G/D = 0.3$; (*c*) St_{01} mode for $L/D = 10$ and $G/D = 0.9$; (*d*) St_{02} mode for $L/D = 10$ and $G/D = 0.9$. (*a*) The values are ± 0.0001; (*b,c,d*) the values are ± 0.0005. The red parts are positive and the blue parts are negative. The arrows mark the periodic topological structures corresponding to streamwise vortices in the gap.

figures 28(*a*) and 28(*b*), indicating competitive coexistence within the LLE shear layer, where St_{01} promotes streamwise vortices and St_{02} suppresses them.

3.4. *Discussion*

In the current FNRC, multiple vortex shedding modes compete, similar to the findings by Chiarini *et al.* (2022*c*) in the FIRC at $Re = 400$. They observed that TE vortex shedding is key to flow locking, while the LE shear layer remains active in instability. Both two flow configurations can be stable under certain conditions, but at $Re = 1000$, vortex shedding tends to be fixed (Li *et al.* 2024*b*). In the present flows, the near-wall effect disrupts symmetry and the feedback loop, particularly affecting the instability position of the LE shear layer and the reattachment point along the cylinder sides. Consequently, these factors disturb the original flow patterns, including the fixed vortex shedding modes across different L/D ratios, leading to the active LE shear layer that facilitates the emergence of multiple vortex shedding modes. Ultimately, this results in instances of mode competition. Chiarini *et al.* (2022*c*) noted that in the FIRC, flow frequency locks onto the LE vortices passing over the TE corners, selecting the configuration with the longest shedding period. Li *et al.* (2024*b*) found that at $Re = 1000$, the shedding pattern is contralateral at $L/D = 10$, differing from ipsilateral shedding at $L/D = 5$ and $L/D = 15$. In this study, alternating TE vortex shedding occurs at $G/D = 0.9$. However, due to flow asymmetry across the cylinder, the contralateral shedding pattern cannot be sustained at $L/D = 10$. This disrupts the feedback loop, preventing the flow from locking onto the LE vortex frequency and selecting the longest shedding period, as seen in the FIRC. Instead, the TE vortex shedding mode at $L/D = 10$ and $G/D = 0.9$ has a shorter period.

Through DMD analysis, the dominant shedding frequencies for each flow are shown in figure 35. For comparison, vortex shedding frequencies from the FIRC at the same Re are also included. The results show that the near-wall effect raises the vortex shedding frequency, promoting vortex shedding. At $L/D = 10$ and $G/D = 0.9$, two dominant frequencies are observed due to suppressed frequency locking. The higher frequency of ULE vortex shedding is similar to the findings of Zhang *et al.* (2023), who reported a

https://doi.org/10.1017/jfm.2025.365 Published online by Cambridge University Press

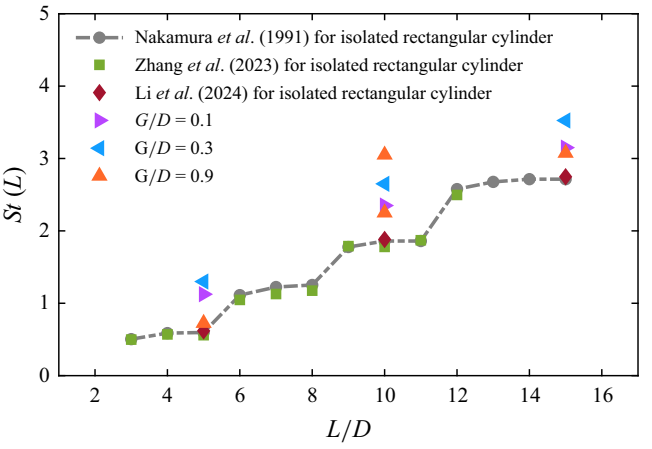


Figure 35. The Strouhal number based on the streamwise dimension of the rectangular cylinder $St(L)$ at different aspect ratios and gap ratios compared with the results for the FIRC from the studies of Nakamura *et al.* (1991), Zhang *et al.* (2023) and Li *et al.* (2024*b*).

higher frequency for LE vortices in the FIRC with a splitter plate, independent of the TE vortex. This is also observed in the present flow. When the LE and TE vortices are no longer locked to the same frequency, the ULE vortex frequency significantly exceeds that of the TE vortex. This higher frequency is also present in the shedding process of the LLE vortex. Focusing on the TE vortex shedding frequency across circular and rectangular cylinders, as G/D increases from 0.1 to 0.3, the wake vortex frequency rises significantly. However, as G/D increases further to 0.9, the frequency decreases. This pattern is consistent across different L/D values. In the FNCC, the shedding frequency increases as G/D decreases from around 2 to 0.5, then decreases further with smaller G/D (Lin *et al.* 2009; He *et al.* 2017; Li *et al.* 2022*a*). According to Jiang *et al.* (2024), the increase in $St(L)$ from $G/D = 0.1$ to 0.3 is due to the plate wall influence, while the decrease from $G/D = 0.3$ to 0.9 is linked to the upstream wall boundary layer development.

4. Conclusion

This study presents a novel investigation into the vortex dynamics of a FNRC using DNS, marking the first comprehensive exploration of these phenomena. By varying the aspect ratios ($L/D = 5$, 10 and 15) and gap ratios ($G/D = 0.1$, 0.3 and 0.9) while maintaining a fixed Re of $Re = 1000$, the study reveals the complex evolution of vortex structures, mean flow topology and frequency characteristics influenced by the near-wall effect. The results demonstrate that both L/D and G/D significantly affect vortex dynamics, leading to the emergence of novel vortex behaviours that are not observed in FIRC or FNCC.

The mean flow topology reveals that smaller gap ratios ($G/D = 0.1$, 0.3) suppress the LLE recirculation, while larger gap ratios ($G/D = 0.9$) promote the formation of a LLE shear layer. The wall-normal scale of the ULE recirculation is smaller than that observed in the FIRC for all flows and increases with G/D, whereas the streamwise scale is larger due to the delayed reattachment. At $L/D = 5$, the ULE recirculation nearly spans the entire upper side of the cylinder for all values of G/D. Reattachment occurs first at $G/D = 0.3$ across all aspect ratios, although the shear intensity of the ULE shear layer decays more rapidly at $G/D = 0.9$. As the cylinder moves farther from the wall, fluctuations gradually increase, reflecting the diminishing influence of the near-wall effect.

https://doi.org/10.1017/jfm.2025.365 Published online by Cambridge University Press

In terms of vortex dynamics, the complexity of the vortex distribution increases as G/D increases. The UKH vortex formed by the ULE shear layer undergoes a transition into the ULE vortex for all cases. At smaller gap ratios, the merging of UKH vortices forms the ULE vortex before undergoing further instability, which contrasts with the dynamics observed in the FIRC. As G/D increases, more intricate vortex shedding modes emerge, with frequency locking observed in most flows. However, this phenomenon is suppressed at $L/D = 10$ and $G/D = 0.9$. The trend in shedding frequency follows a pattern similar to the FNCC: as G/D increases from 0.1 to 0.3, the shedding frequency increases, while a decrease occurs as G/D rises from 0.3 to 0.9. The primary vortex dynamic behaviours at different gap ratios are summarized as follows.

(i) G/$D = 0.1$. The formation of the LTE vortex is suppressed, and alternating vortex shedding is absent. At $L/D = 5$, the UTE vortex is absent, resulting in a direct connection between the ULE recirculation and the downstream wall recirculation. This forms a continuous recirculation, allowing fluid to flow from the downstream region back to the upper side of the cylinder. The ULE vortex at $L/D = 5$ is formed by the merging of two UKH vortices, whereas at larger aspect ratios ($L/D = 10$ and 15), it results from a single UKH vortex.

(ii) G/$D = 0.3$. Similar to $G/D = 0.1$, the formation of the LTE vortex is suppressed, though the dynamics differ from those in the FNCC at the same $G/D = 0.3$. At larger L/D, a novel phenomenon occurs with the emergence of double-TE vortices. Two distinct generation mechanisms for the WPV are identified: for $L/D = 5$, strong wall recirculation leads to the formation of the WPV, which absorbs TSV-induced recirculation; at $L/D = 10$ and 15, the WPV is primarily generated by the gap flow, preventing the absorption of wall recirculation. The UKH vortices continue to merge to form ULE vortices, consistent with the behaviour observed at $G/D = 0.1$.

(iii) G/$D = 0.9$. The LKH vortex (LLE vortex) forms, giving rise to the LSV from the wall, which in turn contributes to the formation of a TV from the lower boundary layer of the cylinder. At $L/D = 5$, the LLE vortex and TV evolve into the LTE vortex and pseudo-TE vortex, respectively. Double-secondary vortices form, consisting of one strong vortex that rises with the LTE vortex into the wake and a weaker vortex that strengthens during this process. A notable observation is that although four UKH vortices are generated, only two of them merge. As L/D increases, the SV signal becomes more pronounced, and the LLE vortex quickly evolves into a streamwise vortex pair, with the TV eventually transforming into the TE vortex. At $L/D = 15$, the LSV develops into hairpin-like vortices, while two UKH vortices merge to form a single ULE vortex, mirroring the behaviour observed in the FIRC. At $L/D = 10$, however, the development of the LSV is influenced by two competing shedding modes with different frequencies: the lower-frequency mode, which governs the TE vortex shedding, promotes the formation of streamwise vortices, while the higher-frequency mode, responsible for ULE vortex shedding, suppresses it. Despite these competing dynamics, the merging of UKH vortices remains consistent with that observed at smaller G/D values.

Ultimately, the study uncovers a range of unique vortex behaviours linked to near-wall effects and provides new insights into the intricate dynamics of vortex shedding in near-wall bluff body flows. The findings are a crucial step forward in understanding vortex formation and interactions in complex flow environments and lay the groundwork for future investigations into the mechanisms of boundary layer transition across varying gap and aspect ratios.

https://doi.org/10.1017/jfm.2025.365 Published online by Cambridge University Press

Funding. The authors acknowledge the financial support of the National Natural Science Foundation of China (52425102, 11972220, 11988102, 52088102, 12032016, 12422208, 12432011, 12421002, 12372277), the China Postdoctoral Science Foundation under grant no. 2024M761953, the Fundamental Research Funds for the Central Universities, National Key Research and Development Program of China (2022YFB2602800, 2023YFC2813103).

Declaration of interests. The authors report no conflict of interest.

References

Basley, J., Pastur, L., Lusseyran, F., Faure, T.M. & Delprat, N. 2011 Experimental investigation of global structures in an incompressible cavity flow using time-resolved PIV. *Exp. Fluids* **50** (4), 905–918.

Bearman, P.W. & Zdravkovich, M.M. 1978 Flow around a circular cylinder near a plane boundary. *J. Fluid Mech.* **89** (1), 33–47.

Bolis, A. 2013 Fourier spectral/hp element method: investigation of time-stepping and parallelisation strategies. *PhD thesis*. Citeseer.

Cantwell, C.D. *et al.* 2015 Nektar++: An open-source spectral/ h p element framework. *Comput. Phys. Commun.* **192**, 205–219.

Chen, W., Ji, C., Alam, M.M., Xu, D. & Zhang, Z. 2022 Three-dimensional flow past a circular cylinder in proximity to a stationary wall. *Ocean Engng* **247**, 110783.

Cheng, H., Jiang, H., Chong, K.L., Zhou, Q., Liu, Y. & Lu, Z. 2022 The effect of surface roughness on the lagrangian coherent structures in turbulent Rayleigh–Bénard convection. *Phys. Fluids* **34** (11), 115134.

Chiarini, A. & Auteri, F. 2023 Linear global and asymptotic stability analysis of the flow past rectangular cylinders moving along a wall. *J. Fluid Mech.* **966**, A22.

Chiarini, A., Gatti, D., Cimarelli, A. & Quadrio, M. 2022*a* Structure of turbulence in the flow around a rectangular cylinder. *J. Fluid Mech.* **946**, A35.

Chiarini, A., Quadrio, M. & Auteri, F. 2022*b* An almost subharmonic instability in the flow past rectangular cylinders. *J. Fluid Mech.* **950**, A20.

Chiarini, A., Quadrio, M. & Auteri, F. 2022*c* On the frequency selection mechanism of the low-*Re* flow around rectangular cylinders. *J. Fluid Mech.* **933**, A44.

Chiarini, A. & Quadrio, M. 2021 The turbulent flow over the barc rectangular cylinder: a DNS study. *Flow Turbul. Combust.* **107** (4), 875–899.

Chiarini, A., Quadrio, M. & Auteri, F. 2021 Linear stability of the steady flow past rectangular cylinders. *J. Fluid Mech.* **929**, A36.

Cimarelli, A., Corsini, R. & Stalio, E. 2024 Reynolds number effects in separating and reattaching flows with passive scalar transport. *J. Fluid Mech.* **984**, A20.

Cimarelli, A., Leonforte, A. & Angeli, D. 2018*a* Direct numerical simulation of the flow around a rectangular cylinder at a moderately high Reynolds number. *J. Wind Engng Ind. Aerodyn.* **174**, 39–49.

Cimarelli, A., Leonforte, A. & Angeli, D. 2018*b* On the structure of the self-sustaining cycle in separating and reattaching flows. *J. Fluid Mech.* **857**, 907–936.

Cimarelli, A., Leonforte, A., Angelis, D.E., Crivellini, E., A, & Angeli, D. 2019*a* On negative turbulence production phenomena in the shear layer of separating and reattaching flows. *Phys. Lett. A* **383** (10), 1019–1026.

Cimarelli, A., Leonforte, A., Angelis, D.E., Crivellini, E., A, & Angeli, D. 2019*b* Resolved dynamics and subgrid stresses in separating and reattaching flows. *Phys. Fluids* **31** (9), 095101.

Dong, S.C., Karniadakis, G.E. & Chryssostomidis, C. 2014 A robust and accurate outflow boundary condition for incompressible flow simulations on severely-truncated unbounded domains. *J. Comput. Phys.* **261**, 83–105.

Dong, S.W., Huang, Y.X., Yuan, X.X. & Lozano-Durán, A. 2020 The coherent structure of the kinetic energy transfer in shear turbulence. *J. Fluid Mech.* **892**, A22.

Dong, Z.-X., Pan, C., Tong, F.-L. & Yuan, X.-X. 2024 Variation of vortical structures across shock-wave/turbulent boundary-layer interaction region in a compression ramp flow. *Phys. Fluids* **36** (5), 055105.

Duan, F. & Wang, J.-J. 2024 Passive bionic motion of a flexible film in the wake of a circular cylinder: chaos and periodicity, flow–structure interactions and energy evolution. *J. Fluid Mech.* **986**, A29.

Fang, X. & Tachie, M.F. 2020 Spatio-temporal dynamics of flow separation induced by a forward-facing step submerged in a thick turbulent boundary layer. *J. Fluid Mech.* **892**, A40.

Feng, S., Tu, G., Yang, Q., Wang, B., Zhou, Q. & Chen, J. 2024 Stability analysis for high-speed boundary-layer flow with cavities. *AIAA J.* **62** (5), 1744–1754.

Green, M.A., Rowley, C.W. & Haller, G. 2007 Detection of lagrangian coherent structures in three-dimensional turbulence. *J. Fluid Mech.* **572**, 111–120.

https://doi.org/10.1017/jfm.2025.365 Published online by Cambridge University Press

HALLER, G. 2001 Distinguished material surfaces and coherent structures in three-dimensional fluid flows. *Physica D* **149** (4), 248–277.

HALLER, G. & YUAN, G. 2000 Lagrangian coherent structures and mixing in two-dimensional turbulence. *Physica D* **147** (3-4), 352–370.

HE, G.-S., PAN, C., FENG, L.-H., GAO, Q. & WANG, J.-J. 2016 Evolution of lagrangian coherent structures in a cylinder-wake disturbed flat plate boundary layer. *J. Fluid Mech.* **792**, 274–306.

HE, G.S., PAN, C. & WANG, J.J. 2013a Dynamics of vortical structures in cylinder/wall interaction with moderate gap ratio. *J. Fluid Struct.* **43**, 100–109.

HE, G.S., WANG, J.J & PAN, C. 2013*b* Initial growth of a disturbance in a boundary layer influenced by a circular cylinder wake. *J. Fluid Mech.* **718**, 116–130.

HE, G.-S., WANG, J.-J., PAN, C., FENG, L.-H., GAO, Q. & RINOSHIKA, A. 2017 Vortex dynamics for flow over a circular cylinder in proximity to a wall. *J. Fluid Mech.* **812**, 698–720.

HOURIGAN, K., THOMPSON, M.C. & TAN, B.T. 2001 Self-sustained oscillations in flows around long blunt plates. *J. Fluids Struct.* **15** (3-4), 387–398.

JIANG, H., HU, X., CHENG, L. & ZHOU, T. 2022 Direct numerical simulation of the turbulent kinetic energy and energy dissipation rate in a cylinder wake. *J. Fluid Mech.* **946**, A11.

JIANG, H., JU, X., GUO, Z. & WANG, L. 2024 Turbulent wake characteristics for a circular cylinder in proximity to a moving wall. *J. Fluid Mech.* **983**, A18.

JIMÉNEZ, J., DEL, A., JUAN, C. & FLORES, O. 2004 The large-scale dynamics of near-wall turbulence. *J. Fluid Mech.* **505**, 179–199.

JU, XG, AN, H., CHENG, L. & TONG, F. 2020 Modes of synchronisation around a near-wall oscillating cylinder in streamwise directions. *J. Fluid Mech.* **893**, A8.

JU, X. & JIANG, H. 2024 Two-and three-dimensional wake transitions of a rectangular cylinder and resultant hydrodynamic effects. *J. Fluid Mech.* **989**, A6.

KUKRETI, S. & SINGH, N.K. 2023 Aspect ratio effect on flow past an elliptical cylinder near a moving wall. *Phys. Fluids* **35** (6), 063606.

LEI, C., CHENG, L., ARMFIELD, S.W. & KAVANAGH, K. 2000 Vortex shedding suppression for flow over a circular cylinder near a plane boundary. *Ocean Engng* **27** (10), 1109–1127.

LEI, C., CHENG, L. & KAVANAGH, K. 1999 Re-examination of the effect of a plane boundary on force and vortex shedding of a circular cylinder. *J. Wind Engng Ind. Aerodyn.* **80** (3), 263–286.

LI, J., WANG, B., QIU, X., WU, J., ZHOU, Q., FU, S. & LIU, Y. 2022*a* Three-dimensional vortex dynamics and transitional flow induced by a circular cylinder placed near a plane wall with small gap ratios. *J. Fluid Mech.* **953**, A2.

LI, J.-H., WANG, B.-F., QIU, X., WU, J.-Z., ZHOU, Q., FU, S.-X. & LIU, Y.-L. 2022*b* The dynamics of cylinder-wake/boundary-layer interaction revealed by turbulent transports. *Phys. Fluids* **34** (11), 115136.

LI, J.-H., WANG, B.-F., QIU, X., ZHOU, Q., FU, S.-X. & LIU, Y.-L. 2024*a* Turbulent transports in the flow around a rectangular cylinder with different aspect ratios. *Ocean Engng* **301**, 117512.

LI, J.-H., WANG, B.-F., QIU, X., ZHOU, Q., FU, S.-X. & LIU, Y.-L. 2024*b* Vortex dynamics and boundary layer transition in flow around a rectangular cylinder with different aspect ratios at medium Reynolds number. *J. Fluid Mech.* **982**, A5.

LI, Z., ZHANG, D., LIU, Y., WU, C. & GAO, N. 2020 Effect of periodic perturbations on the turbulence statistics in a backward-facing step flow. *Phys. Fluids* **32** (7), 075116.

LI, Z.-F., LI, J.-H., WU, J.-Z., CHONG, K.-L., WANG, B.-F., ZHOU, Q. & LIU, Y.-L. 2023 Numerical simulation of flow instability induced by a fixed cylinder placed near a plane wall in oscillating flow. *Ocean Engng* **288**, 116115.

LIN, W.J., LIN, C., HSIEH, S.C. & DEY, S. 2009 Flow characteristics around a circular cylinder placed horizontally above a plane boundary. *J. Engng Mech.* **135** (7), 697–716.

LIU, Y., WANG, Y., LI, J., TAO, Y. & QIU, X. 2022 Experimental study on the large-scale turbulence structure dynamics of a counterflowing wall jet. *Exp. Fluids* **63** (10), 159.

MA, L.-Q., FENG, L.-H., PAN, C., GAO, Q. & WANG, J.-J. 2015 Fourier mode decomposition of PIV data. *China Technol. Sci.* **58** (11), 1935–1948.

MA, X. & SCHRÖDER, A. 2017 Analysis of flapping motion of reattaching shear layer behind a two-dimensional backward-facing step. *Phys. Fluids* **29** (11), 115104.

MA, X., TANG, Z. & JIANG, N. 2020 Eulerian and lagrangian analysis of coherent structures in separated shear flow by time-resolved particle image velocimetry. *Phys. Fluids* **32** (6), 065101.

MAHMOODI-JEZEH, S.V. & WANG, B.-C. 2020 Direct numerical simulation of turbulent flow through a ribbed square duct. *J. Fluid Mech.* **900**, A18.

MAITI, D.K. 2012 Numerical study on aerodynamic characteristics of rectangular cylinders near a wall. *Ocean Engng* **54**, 251–260.

https://doi.org/10.1017/jfm.2025.365 Published online by Cambridge University Press

MALAVASI, S. & BLOIS, G. 2012 Wall effects on the flow structure around a rectangular cylinder. *Meccanica* **47** (4), 805–815.

MILLS, R., SHERIDAN, J. & HOURIGAN, K. 2002 Response of base suction and vortex shedding from rectangular prisms to transverse forcing. *J. Fluid Mech.* **461**, 25–49.

MILLS, R., SHERIDAN, J., HOURIGAN, K. & WELSH, M.C. 1995 The mechanism controlling vortex shedding from rectangular bluff bodies. In *Proceeding Twelfth Australas. Fluid Mechanica Conference*, pp. 227–230.

MOSER, R.D. & MOIN, P. 1987 The effects of curvature in wall-bounded turbulent flows. *J. Fluid Mech.* **175**, 479–510.

MOXEY, D. *et al.* 2020 Nektar++: enhancing the capability and application of high-fidelity spectral/hp element methods. *Comput. Phys. Commun.* **249**, 107110.

NAKAMURA, Y. & NAKASHIMA, M. 1986 Vortex excitation of prisms with elongated rectangular, h and [vdash] cross-sections. *J. Fluid Mech.* **163**, 149–169.

NAKAMURA, Y., OHYA, Y. & TSURUTA, H. 1991 Experiments on vortex shedding from flat plates with square leading and trailing edges. *J. Fluid Mech.* **222**, 437–447.

NAUDASCHER, E. & ROCKWELL, D. 1994 Flow-induced vibrations: An engineering guide.

OKAJIMA, A. 1982 Strouhal numbers of rectangular cylinders. *J. Fluid Mech.* **123**, 379–398.

OURO, P., MUHAWENIMANA, V. & WILSON, C.A. 2019 Asymmetric wake of a horizontal cylinder in close proximity to a solid boundary for reynolds numbers in the subcritical turbulence regime. *Phys. Rev. Fluids* **4** (10), 104604.

OVCHINNIKOV, V., PIOMELLI, U. & CHOUDHARI, M.M. 2006 Numerical simulations of boundary-layer transition induced by a cylinder wake. *J. Fluid Mech.* **547**, 413–441.

OZONO, S., OHYA, Y., NAKAMURA, Y. & NAKAYAMA, R. 1992 Stepwise increase in the Strouhal number for flows around flat plates. *Intl J. Numer. Meth. Fluids* **15** (9), 1025–1036.

PAN, C., WANG, J., WANG, J. & SUN, M. 2017 Dynamics of an unsteady stagnation vortical flow via dynamic mode decomposition analysis. *Exp. Fluids* **58** (3), 1–19.

PRICE, S.J., SUMNER, D., SMITH, J.G., LEONG, K. & PAIDOUSSIS, M.P. 2002 Flow visualization around a circular cylinder near to a plane wall. *J. Fluid Struct.* **16** (2), 175–191.

REN, C., LIU, Z., CHENG, L., TONG, F. & XIONG, C. 2023 Three-dimensional wake transitions of steady flow past two side-by-side cylinders. *J. Fluid Mech.* **972**, A17.

SARKAR, S. & SARKAR, S. 2009 Large-eddy simulation of wake and boundary layer interactions behind a circular cylinder. *Trans. ASME J. Fluids Engng* **131** (9), 091201.

SARKAR, S. & SARKAR, S. 2010 Vortex dynamics of a cylinder wake in proximity to a wall. *J. Fluid Struct.* **26** (1), 19–40.

SCHMID, P.J. 2010 Dynamic mode decomposition of numerical and experimental data. *J. Fluid Mech.* **656**, 5–28.

SHADDEN, S.C., ASTORINO, M. & GERBEAU, J.-F. 2010 Computational analysis of an aortic valve jet with Lagrangian coherent structures. *Chaos* **20** (1), 017512.

SHADDEN, S.C., DABIRI, J.O. & MARSDEN, J.E. 2006 Lagrangian analysis of fluid transport in empirical vortex ring flows. *Phys. Fluids* **18** (4), 047105.

SQUIRE, L.C. 1989 Interactions between wakes and boundary-layers. *Prog. Aerosp. Sci.* **26** (3), 261–288.

TAN, B., THOMPSON, M. & HOURIGAN, K. 2004 Flow past rectangular cylinders: receptivity to transverse forcing. *J. Fluid Mech.* **515**, 33–62.

TAN, B.T., THOMPSON, M. & HOURIGAN, K. 1998 Simulated flow around long rectangular plates under cross flow perturbations. *Intl J. Fluid Dyn.* **2**, 1.

TANWEER, S., DEWAN, A. & SANGHI, S. 2021 Three-dimensional wake transitions past a rectangular cylinder placed near a moving wall: influence of aspect and gap ratios. *Ocean Engng* **219**, 108288.

TANWEER, S., DEWAN, A. & SANGHI, S. 2022 Flow dynamics in the wake of a rectangular cylinder near a moving wall. *Ocean Engng* **266**, 112966.

TIAN, R., XU, Y., DUAN, F. & WANG, J.-J. 2023 The deformation and dynamics of a flexible plate with attached mass blocks mounted behind a circular cylinder. *J. Fluid Struct.* **122**, 103979.

WANG, J., HE, G. & WANG, J. 2024 Revisiting the wake-triggered secondary vortices over a circular-cylinder/flat-plate configuration. *Phys. Fluids* **36** (2), 021704.

WANG, J., WANG, J. & KIM, K.C. 2019 Wake/shear layer interaction for low-Reynolds-number flow over multi-element airfoil. *Exp. Fluids* **60** (1), 1–24.

WANG, J.-S., FENG, L.-H., WANG, J.-J. & LI, T. 2018 Görtler vortices in low-Reynolds-number flow over multi-element airfoil. *J. Fluid Mech.* **835**, 898–935.

WANG, J.S., GAO, Q., WEI, R.J. & WANG, J.J. 2017 Experimental study on the effect of an artificial cardiac valve on the left ventricular flow. *Exp. Fluids* **58** (9), 1–17.

https://doi.org/10.1017/jfm.2025.365 Published online by Cambridge University Press

WANG, J.-S. & WANG, J.-J. 2021*a* Vortex dynamics for flow around the slat cove at low Reynolds numbers. *J. Fluid Mech.* **919**, A27.

WANG, J.-S. & WANG, J.-J. 2021*b* Wake-induced transition in the low-Reynolds-number flow over a multi-element airfoil. *J. Fluid Mech.* **915**, A28.

WANG, J.-S., WU, J. & WANG, J.-J. 2023 Wake-triggered secondary vortices over a cylinder/airfoil configuration. *Exp. Fluids* **64** (1), 6.

WANG, L., PAN, C., WANG, J. & GAO, Q. 2022*a* Statistical signatures of component wall-attached eddies in proper orthogonal decomposition modes of a turbulent boundary layer. *J. Fluid Mech.* **944**, A26.

WANG, L.-W., PAN, C. & WANG, J.-J. 2022*b* Wall-attached and wall-detached eddies in proper orthogonal decomposition modes of a turbulent channel flow. *Phys. Fluids* **34** (9), 095124.

WANG, X.K. & TAN, S.K. 2008 Near-wake flow characteristics of a circular cylinder close to a wall. *J. Fluid Struct.* **24** (5), 605–627.

ZDRAVKOVICH, M.M. 1985 Forces on a circular cylinder near a plane wall. *Appl. Ocean Res.* **7** (4), 197–201.

ZHANG, L.-R., LI, J.-H., WANG, Y.-Z., QIU, X., FU, Y. & LIU, Y.-L. 2024 Vortex dynamics induced by a finite wall-mounted cylinder with various corner shapes. *Phys. Fluids* **36** (7), 075195.

ZHANG, Z., KAREEM, A., XU, F. & JIANG, H. 2023 Global instability and mode selection in flow fields around rectangular prisms. *J. Fluid Mech.* **955**, A19.

ZHOU, J., QIU, X., LI, J. & LIU, Y. 2022 Vortex evolution of flow past the near-wall circular cylinder immersed in a flat-plate turbulent boundary layer. *Ocean Engng* **260**, 112011.

ZHOU, J., QIU, X., LI, J., WANG, B., ZHOU, Q. & LIU, Y. 2024 The experimental investigation on wake dynamics of flow around a circular cylinder with the splitter plate. *J. Fluid Struct.* **127**, 104130.

ZHOU, Y., NAGATA, K., SAKAI, Y., ITO, Y. & HAYASE, T. 2015 On the evolution of the invariants of the velocity gradient tensor in single-square-grid-generated turbulence. *Phys. Fluids* **27** (7), 075107.

ZHOU, Y., NAGATA, K., SAKAI, Y. & WATANABE, T. 2019 Extreme events and non-Kolmogorov spectra in turbulent flows behind two side-by-side square cylinders. *J. Fluid Mech.* **874**, 677–698.

https://doi.org/10.1017/jfm.2025.365 Published online by Cambridge University Press